The Astrophysical Journal, 737:13 (17pp), 2011 August 10 doi:10.1088/0004-637X/737/1/13

COMPARING NUMERICAL METHODS FOR ISOTHERMAL MAGNETIZED SUPERSONIC TURBULENCE

Alexei G. Kritsuk[1,2], Åke Nordlund[2,3], David Collins[1,2,4], Paolo Padoan[2,5], Michael L. Norman[1,6], Tom Abel[2,7], Robi Banerjee[2,3,9], Christoph Federrath[8,10,11], Mario Flock[10], Dongwook Lee[12], Pak Shing Li[2,13], Wolf-Christian Müller[14], Romain Teyssier[2,15,16], Sergey D. Ustyugov[17], Christian Vogel[14], and Hao Xu[1,3]

[1] Physics Department and Center for Astrophysics and Space Sciences, University of California, San Diego, La Jolla, CA 92093-0424, USA; akritsuk@ucsd.edu
[2] Kavli Institute for Theoretical Physics, University of California, Santa Barbara, CA 93106-4030, USA
[3] Centre for Star and Planet Formation and Niels Bohr Institute, University of Copenhagen, DK-2100, Copenhagen, Denmark; aake@nbi.dk
[4] Theoretical Division, Los Alamos National Laboratory, Los Alamos, NM 87545, USA; dccollins@lanl.gov, hao_xu@lanl.gov
[5] ICREA & ICC, University of Barcelona, E-08028, Barcelona, Spain; ppadoan@icc.ub.edu
[6] San Diego Supercomputer Center, University of California, San Diego, La Jolla, CA 92093-0505, USA; mlnorman@ucsd.edu
[7] Kavli Institute for Particle Astrophysics and Cosmology, Stanford Linear Accelerator Center and Stanford Physics Department, Menlo Park, CA 94025, USA; tabel@stanford.edu
[8] Zentrum für Astronomie der Universität Heidelberg, Institut für Theoretische Astrophysik, D-69120 Heidelberg, Germany; chfeder@ita.uni-heidelberg.de
[9] Hamburger Sternwarte, D-21029 Hamburg, Germany; banerjee@hs.uni-hamburg.de
[10] Max-Planck-Institute for Astronomy, D-69117 Heidelberg, Germany; flock@mpia.de
[11] École Normale Supérieure de Lyon, CRAL, 69364 Lyon, France
[12] FLASH Center for Computational Science, Chicago, IL 60637, USA; dongwook@flash.uchicago.edu
[13] Astronomy Department, University of California, Berkeley, CA 94720, USA; psli@berkeley.edu
[14] Max-Planck-Institut für Plasmaphysik, D-85748 Garching, Germany; Wolf.Mueller@ipp.mpg.de, cvogel@ipp.mpg.de
[15] CEA, IRFU, SAp. F-91191 Gif-sur-Yvette, France; romain.teyssier@cea.fr
[16] Institute of Theoretical Physics, University of Zurich, 8057 Zurich, Switzerland
[17] Keldysh Institute for Applied Mathematics, Russian Academy of Sciences, Moscow 125047, Russia; ustyugs@keldysh.ru
Received 2011 March 28; accepted 2011 May 12; published 2011 July 22

ABSTRACT

Many astrophysical applications involve magnetized turbulent flows with shock waves. Ab initio star formation simulations require a robust representation of supersonic turbulence in molecular clouds on a wide range of scales imposing stringent demands on the quality of numerical algorithms. We employ simulations of supersonic super-Alfvénic turbulence decay as a benchmark test problem to assess and compare the performance of nine popular astrophysical MHD methods actively used to model star formation. The set of nine codes includes: ENZO, FLASH, KT-MHD, LL-MHD, PLUTO, PPML, RAMSES, STAGGER, and ZEUS. These applications employ a variety of numerical approaches, including both split and unsplit, finite difference and finite volume, divergence preserving and divergence cleaning, a variety of Riemann solvers, and a range of spatial reconstruction and time integration techniques. We present a comprehensive set of statistical measures designed to quantify the effects of numerical dissipation in these MHD solvers. We compare power spectra for basic fields to determine the effective spectral bandwidth of the methods and rank them based on their relative effective Reynolds numbers. We also compare numerical dissipation for solenoidal and dilatational velocity components to check for possible impacts of the numerics on small-scale density statistics. Finally, we discuss the convergence of various characteristics for the turbulence decay test and the impact of various components of numerical schemes on the accuracy of solutions. The nine codes gave qualitatively the same results, implying that they are all performing reasonably well and are useful for scientific applications. We show that the best performing codes employ a consistently high order of accuracy for spatial reconstruction of the evolved fields, transverse gradient interpolation, conservation law update step, and Lorentz force computation. The best results are achieved with divergence-free evolution of the magnetic field using the constrained transport method and using little to no explicit artificial viscosity. Codes that fall short in one or more of these areas are still useful, but they must compensate for higher numerical dissipation with higher numerical resolution. This paper is the largest, most comprehensive MHD code comparison on an application-like test problem to date. We hope this work will help developers improve their numerical algorithms while helping users to make informed choices about choosing optimal applications for their specific astrophysical problems.

Key words: ISM: structure – magnetohydrodamics (MHD) – methods: numerical – turbulence

1. INTRODUCTION

It is well established that the observed supersonic turbulence plays an important role in the fragmentation of molecular clouds leading to star formation (Mac Low & Klessen 2004; McKee & Ostriker 2007). As illustrated by numerical simulations, random supersonic flows in an isothermal gas result in a complex network of shocks creating a filamentary density structure with a very large density contrast (e.g., Kritsuk et al. 2007; Federrath et al. 2008, see also references in Klessen et al. 2009; Pudritz 2011). Because it can naturally generate density enhancements of sufficient amplitude to allow the formation of low-mass stars or even brown dwarfs within complex layers of post-shock gas, the turbulence may directly affect the mass distribution of pre-stellar cores and stars (Padoan & Nordlund 2002; Padoan et al. 2007; Hennebelle & Chabrier 2008, 2009). Furthermore, the turbulence must be at least partly responsible for the low star formation rate per free-fall time observed in most environments (Krumholz & Tan 2007) because the turbulent energy generally exceeds the gravitational energy on small scales within molecular clouds (the virial parameter is almost always larger than unity, as shown by Falgarone et al. 1992

and Rosolowsky et al. 2009 in Perseus). Theoretical models of the star formation rate based on the effect of turbulence have recently been proposed (Krumholz & McKee 2005; Padoan & Nordlund 2011).

The importance of turbulence in the process of star formation provides an opportunity for theoretical modeling because one can assume that molecular clouds follow the universal statistics of turbulent flows, for example, with respect to the probability density function (PDF) of gas density and the scaling of velocity differences. Turbulence is also a challenge for numerical simulations of star formation because the limited dynamical range of the simulations cannot always approximate well enough the scale-free behavior of the turbulent flow. The Kolmogorov dissipation scale, $\eta_{\rm K}$, is the smallest turbulent scale below which viscous dissipation becomes dominant. It can be computed as $\eta_{\rm K} = (\nu^3/\epsilon)^{1/4}$, where ν is the kinematic viscosity and ϵ is the mean dissipation rate of the turbulence. The kinematic viscosity can be approximated as $\nu \approx \upsilon_{\rm th}/(\sigma n)$, where $\upsilon_{\rm th}$ is the gas thermal velocity, n is the gas mean number density, and $\sigma \approx 5 \times 10^{-15}$ cm^2 is the gas collisional cross section. The mean dissipation rate can be estimated as $\epsilon \sim \upsilon^3/\ell$, where ℓ is a scale within the inertial range of the turbulence, and υ is the rms velocity at the scale ℓ. In molecular clouds, assuming the Larson (1981) relations $\upsilon \sim 1$ km s^{-1} $(\ell/1\ {\rm pc})^{0.42}$ and $n \sim 10^3$ cm^{-3} $(\ell/1\ {\rm pc})^{-1}$, a gas temperature of 10 K, and a driving scale of $\sim$70 pc, we obtain $\eta_{\rm K} \sim 10^{14}$ cm, which is well below the characteristic spatial resolution of the gas dynamics in star formation simulations.

The dynamic range limitation of the simulations can be expressed in terms of the Reynolds number. The Reynolds number estimates the relative importance of the nonlinear advection term and the viscosity term in the Navier–Stokes equation, ${\rm Re} = \upsilon_{\rm rms}\mathcal{L}/\nu$, where $\upsilon_{\rm rms} \equiv \sqrt{\langle \upsilon^2 \rangle}$ is the flow rms velocity, $\mathcal{L}$ is the integral scale of the turbulence (of the order of the energy injection scale). The Reynolds number can also be expressed as ${\rm Re} = (\mathcal{L}/\eta_{\rm K})^{4/3}$. Based on the same assumptions used above to derive $\eta_{\rm K}$, we obtain ${\rm Re} \sim 10^8$ for typical molecular cloud values. At present, the largest simulations of supersonic turbulence may achieve an effective Reynolds number ${\rm Re} \sim 10^4$ (Kritsuk et al. 2009a; Jones et al. 2011).

Numerical simulations are incapable of describing the smallest structures of magnetic fields in star-forming clouds. The characteristic magnetic diffusivity, η, of the cold interstellar gas is much smaller than the kinematic viscosity, ν. As a result, magnetic fields can develop complex structures on scales much smaller than the Kolmogorov dissipation scale, $\eta_{\rm K}$, where the velocity field is smooth. Introducing the magnetic Prandtl number, Pm, defined as the ratio of viscosity and diffusivity, ${\rm Pm} = \nu/\eta$, this regime is characterized by the condition ${\rm Pm} \gg 1$. The magnetic diffusivity can be expressed as $\eta = c^2 m_{\rm e} \nu_{\rm en}/4\pi n_{\rm e} e^2$ (cgs), where c is the speed of light, $m_{\rm e}$ is the electron mass, $\nu_{\rm en}$ is the collision frequency of electrons with neutrals, $n_{\rm e}$ is the number density of electrons, and e is the electron charge. This expression neglects electron–ion collisions because at the low ionization fractions and temperatures of molecular clouds the dominant friction force on the electrons is from collisions with neutrals. The collision frequency of electrons with neutrals can be written as $\nu_{\rm en} = n_{\rm n}\sigma\upsilon_{\rm th,e}$, where $n_{\rm n}$ is the number density of neutrals ($\sim n$ in molecular clouds), σ is the gas collision cross section given above, and $\upsilon_{\rm th,e}$ is the thermal velocity of the electrons. The magnetic Prandtl number is then given by ${\rm Pm} \approx 2 \times 10^5 (x_{\rm i}/10^{-7})(n/1000\ {\rm cm}^{-3})^{-1}$, where $x_{\rm i}$ is the ionization fraction.

Numerical simulations without explicit viscosity and magnetic diffusivity usually have effective values of ${\rm Pm} \sim 1$, very far from the conditions in molecular clouds. If the magnetic field strength is determined self-consistently by a small-scale turbulent dynamo, this numerical limitation may cause an artificially low magnetic field strength in low-resolution simulations, or in simulations based on MHD solvers with large effective magnetic diffusivity. Such simulations may not reach the critical value of the magnetic Reynolds number, Rm, required by the turbulent dynamo. The magnetic Reynolds number is defined as ${\rm Rm} = {\rm RePm} = \upsilon_{\rm rms}\mathcal{L}/\eta$. Its critical value for the turbulent dynamo in supersonic turbulence was found to be ${\rm Rm}_{\rm crit} \approx 80$ in the regime with ${\rm Pm} \sim 1$ and for a sonic rms Mach number $M_{\rm s} \approx 2.5$, where $M_{\rm s} = \upsilon_{\rm rms}/c_{\rm s}$ is the ratio of the flow rms velocity and the speed of sound (Haugen et al. 2004). Federrath et al. (2011) find ${\rm Rm}_{\rm crit} \approx 40$ for transonic turbulence, driven by the gravitational collapse of a dense, magnetized gas cloud.

Besides the effective Re and Pm, the other two nondimensional parameters of isothermal MHD turbulent simulations are the rms sonic Mach number, defined above, and the rms Alfvénic Mach number, $M_{0,\rm A} = \upsilon_{\rm rms}/\upsilon_{0,\rm A}$, where $\upsilon_{0,\rm A}$ is the mean Alfvén speed defined as $\upsilon_{0,\rm A} = B_0/\sqrt{4\pi\rho_0}$, and B_0 and ρ_0 are the mean magnetic field and mean gas density, respectively. The initial conditions of the numerical test described in this work have $M_{\rm s} \approx 9$ and $M_{0,\rm A} \approx 30$. In the test runs, the value of $M_{\rm s}$ decreases with time (no driving force is used), as shown in the left panels of Figure 1. $\upsilon_{0,\rm A}$ is instead constant because both B_0 and ρ_0 are conserved quantities in the simulations. However, the rms value of the magnetic field strength, $\sqrt{\langle B^2 \rangle}$, depends on both B_0 and $\upsilon_{\rm rms}$. In these simulations B_0 is very low, and the turbulence is highly super-Alfvénic, meaning that $\upsilon_{\rm rms} \gg \upsilon_{0,\rm A}$. In this regime, the magnetic field is locally amplified by compression and stretching resulting in a statistically steady state with $\sqrt{\langle B^2 \rangle} \gg B_0$. The rms Alfvénic Mach number defined in terms of the mean magnetic and kinetic energies, $M_{\rm A} = \sqrt{\langle \rho \upsilon^2 \rangle / \langle B^2/4\pi \rangle} \approx 4.4$ and decreases with time as the turbulence decays, as shown by the right panels of Figure 1.

Based on the observed dependence of velocity dispersion on spatial scale in molecular clouds (e.g., Larson 1981; Heyer & Brunt 2004), the initial value of $M_{\rm s}$ in our test runs is relevant to star-forming regions on scales of a few parsecs. The super-Alfvénic nature of molecular cloud turbulence was suggested by Padoan & Nordlund (1999), and has received further support in more recent work (Lunttila et al. 2008, 2009; Padoan et al. 2010; Kritsuk et al. 2011).

One way to assess the ability of numerical simulations to approximate the behavior of turbulent flows is to study the power spectra of relevant quantities, such as velocity and magnetic fields. The interpretation of velocity power spectra from numerical simulations face the following problems: (1) the limited extent of the inertial range of turbulence due to the limited range of spatial scales discussed above (or even the complete absence of an inertial range in the case of low resolution simulations), (2) the emergence of the bottleneck effect in hydrodynamic simulations (e.g., Falkovich 1994; Dobler et al. 2003; Haugen & Brandenburg 2004) as soon as the numerical resolution is large enough to generate an inertial range, (3) the dependence of the power spectrum on the numerical schemes, and (4) the dependence of the numerical resolution necessary for convergence on the numerical method.

This work addresses the above problems and the general issue of the quality of MHD codes with respect to the description

of highly supersonic and super-Alfvénic isothermal turbulent flows. We do not study the quality of simulations of the gravitational collapse of gravitationally unstable regions with adaptive mesh refinement (AMR) or Lagrangian methods in this paper. Although most star formation simulations eventually take advantage of such techniques, here we focus on the simulations of turbulent flows where gravity is neglected. This work considers high-resolution simulations of MHD turbulence, while related studies of nonmagnetized flows have been recently published by Kitsionas et al. (2009) and Price & Federrath (2010).

The paper is organized as follows. In Section 2, we describe the simulation setup. In Section 3, we introduce the algorithms used. In Section 4, we discuss the diagnostic techniques utilized in the paper. In Section 5 we present the results from each code, and in Section 6 we discuss the impact of method design on the numerical dissipation properties. Finally, Section 7 summarizes our conclusions.

2. THE TURBULENCE DECAY TEST PROBLEM

Modern numerical methods for astrophysical turbulence simulations are designed to produce approximations to the limit of viscous and resistive solutions as the viscosity and magnetic diffusivity are reduced to zero. Numerical experiments carried out with such methods can be viewed as implicit large eddy simulations, or ILES (Grinstein et al. 2007). Sytine et al. (2000) demonstrated that Euler solvers, like PPM (Colella & Woodward 1984), are more efficient than Navier–Stokes solvers in providing a better scale separation at a given grid resolution (see also Benzi et al. 2008). Here we employ the same ILES technique for MHD simulations of decaying supersonic turbulence. The numerical methods we compare differ in their implicit subgrid models and the focus of this paper is on understanding the origin of those differences, which could help to improve our methods.

We thus numerically solve the system of MHD equations for an ideal isothermal gas in a cubic domain of size L with periodic boundary conditions:

$$\frac{\partial \rho}{\partial t} + \nabla \cdot (\rho \mathbf{u}) = 0, \tag{1}$$

$$\frac{\partial \rho \mathbf{u}}{\partial t} + \nabla \cdot \left[\rho \mathbf{u}\mathbf{u} - \mathbf{B}\mathbf{B} + \left(p + \frac{\mathbf{B}^2}{2} \right) \mathbf{I} \right] = \rho \mathbf{F}, \tag{2}$$

$$\frac{\partial \mathbf{B}}{\partial t} + \nabla \cdot (\mathbf{u}\mathbf{B} - \mathbf{B}\mathbf{u}) = \mathbf{0}. \tag{3}$$

Here, ρ and $\mathbf{u}$ are the gas density and velocity, $\mathbf{B}$ is the magnetic field strength, p is the gas pressure, and $\mathbf{I}$ is the unit tensor.

All numerical methods discussed in this paper are designed to conserve mass, momentum, and magnetic flux, and attempt to keep $\nabla \cdot \mathbf{B} = 0$ to machine precision. All methods are formulated to approximate the ideal MHD Equations (1)–(3). However, due to the finite numerical viscosity and magnetic diffusivity, as well as artificial viscosity and diffusivity added for numerical concerns, the actual equations evolved will have additional dissipation terms on (2) and (3). The exact nature of these dissipation terms is method-dependent.

In this section and below, we use dimensionless code units, such that the domain size $L = 1$; the gas density ρ is given in units of the mean gas density ρ_0, the gas pressure p is given in units of uniform initial pressure p_0, and the velocity $\mathbf{u}$ is given in units of the sound speed, $u = v/c_s$. The uniform mean magnetic field is $B_0 = \sqrt{2/\beta_0} = 0.3$, where the ratio of thermal-to-magnetic pressure $\beta_0 = 22$. The code units also imply that $\mathbf{B}$ incorporates the $1/4\pi$ factor so that the magnetic pressure is given by $B^2/2$ in the code units.

Initial conditions for the decay test were generated in 2007 with an earlier, non-conservative version of the STAGGER code on a 1000^3 grid using a time-dependent random large-scale ($k/k_{\rm min} \leqslant 2$, where $k_{\rm min} = 2\pi/L$) isotropic solenoidal force (acceleration) $\mathbf{F}$ to stir the gas and reach an rms sonic Mach number $M_{\rm s,0} \approx 9$. There was no forcing in the induction Equation (3), so the rms magnetic field was passively amplified through interaction with the velocity field. The model was initiated with a uniform density ρ_0 and pressure p_0, random large-scale velocity field $\mathbf{u}_0$, and a uniform magnetic field $\mathbf{B}_0$ aligned with the z-coordinate direction. To achieve a saturated turbulent state, the flow was evolved with the STAGGER code for three dynamical times (defined as $t_{\rm d} \equiv L/2M_{\rm s,0}$). Assuming an initial $M_{\rm s,0} = 10$, $t_{\rm d} = 0.05$ in the code units determined by the box sound crossing time. In the saturated turbulent state, the level of magnetic fluctuations is $\sim$50 times higher than B_0, i.e., $\mathbf{B} = \mathbf{B}_0 + \mathbf{b}$, where $b_{\rm rms} \gg B_0$ and $\langle \mathbf{b} \rangle \equiv \mathbf{0}$.

The actual test runs were performed at grid resolutions of 256^3, 512^3, and in a few cases (PPML and ZEUS) also 1024^3 cells. Data regridding utilized conservative interpolation of hydrodynamic variables while a vanishing $\nabla \cdot \mathbf{B}$ in the interpolated initial states was enforced with $\nabla \cdot \mathbf{B}$ cleaning. The evolution of decaying turbulence ($\mathbf{F} \equiv \mathbf{0}$) was followed for $\Delta t = 0.2 = 4t_{\rm d}$ and 10 flow snapshots equally spaced in time were recorded for subsequent analysis. The timing of these snapshots in the adopted time units is as follows: $t_1 = 0.02$, $t_2 = 0.04, \ldots, t_{10} = 0.2$, assuming $t = 0$ corresponds to the end of the initial forcing period.

3. NUMERICAL METHODS AND IMPLEMENTATIONS

3.1. ENZO 2.0

ENZO's (O'Shea et al. 2005) MHD scheme (Wang & Abel 2009) employs the following components: second-order spatial interpolation via the Piecewise Linear Method (van Leer 1979), second-order time integration via a second-order Runge–Kutta method (Shu & Osher 1988), the HLL Riemann solver for computation of interface fluxes (Harten et al. 1983), and the Dedner et al. (2002) scheme for maintaining the divergence of the magnetic field close to zero. The code is formally second-order accurate in both time and space. These one-dimensional components are combined to form a three-dimensional method in a directionally unsplit manner, with the Runge–Kutta integration mediating the wave information between the three flux computations. The slope limiter θ, which controls the sharpness of the reconstruction, was set at 1.5 as in Wang et al. 2008. Larger values were tried for 256^3 grids, without significant change to the solution.

3.2. FLASH 3

The FLASH3 (Fryxell et al. 2000; Dubey et al. 2008) simulations presented in this study have used a completely new MHD scheme implementation (Lee & Deane 2009). The solver adopts a dimensionally unsplit integration on a staggered grid (unsplit staggered mesh (USM)), for the multidimensional MHD formulation, based on a finite-volume, higher-order Godunov method. A new second-order data reconstruction-evolution method, extended from the corner transport upwind (CTU) approach of Colella (1990) has been used, which guarantees proper evolution

of in-plane dynamics of magnetic fields. The importance of the in-plane field evolution is described and tested in the field-loop advection test in Gardiner & Stone (2005). The USM solver has also shown a successful performance on this test, maintaining a correct in-plane field dynamics (Lee & Deane 2009). The algorithm uses a new "multidimensional characteristics analysis" to calculate transverse fluxes. This approach is advantageous and efficient because it does not require solving a set of Riemann problems for updating transverse fluxes. High Mach number turbulent flows require a precise and positive-preserving solver capable of resolving complex shock structures while keeping numerical diffusion as small as possible. We therefore chose the HLLD Riemann solver (Miyoshi & Kusano 2005), which greatly improves the robustness and accuracy of supersonic MHD turbulence simulations as the Roe solver easily fails to preserve positive states of density and/or pressure in strong rarefaction waves. For further enhancing solution accuracy and stability, we chose a hybrid limiter that uses the compressive van Leer's slope limiter for linearly degenerate waves and the more diffusive minmod limiter for genuinely nonlinear waves.

3.3. KT-MHD

The KT-MHD code is an implementation of a semidiscrete central-difference scheme developed by Kurganov & Tadmor (2000). The total time derivative of the hydrodynamic quantities is computed using the flux definition of the Kurganov–Tadmor scheme, a higher-order extension of the Lax–Friedrichs scheme. The flux values are evaluated at the cell interfaces. The corresponding point values of the conserved quantities are interpolated to the cell interfaces via a third-order CWENO scheme in three space dimensions following Balbas & Tadmor (2006). The averages of the magnetic field components reside at the cell interfaces and are reconstructed in a diagonal direction, also using a third-order CWENO scheme. The smoothness indicators (and thereby the nonlinear weights) of the CWENO scheme are based on the density field only. Components-wise smoothness indicators have shown to lead to a much higher numerical viscosity. The total time derivative of the magnetic field is computed by the constrained transport (CT) method of Ziegler (2004). The resulting set of ordinary differential equations is integrated in time by a fourth-order Runge–Kutta scheme. The code uses a regular grid and the so-called pencil decomposition in its MPI-parallel implementation. The idea of combining the Kurganov–Tadmor central-difference scheme with a CT method for the magnetic field update was first implemented by Ralf Kissmann and published in his PhD thesis (Kissmann 2006) and is used by Dreher & Grauer (2005) in their Racoon code.

3.4. LL-MHD

The CT-based LL-MHD solver (Collins et al. 2010) employs the divergence preserving higher-order Godunov method of Li et al. (2008), which uses second-order spatial reconstruction and second-order time reconstruction to compute the interface states, and the isothermal HLLD Riemann solver of Mignone (2007) to compute the flux from those reconstructed states. This is done in a directionally split fashion, with the order permutation of Strang to preserve the second-order accuracy. The solver uses the CT method of Gardiner & Stone (2005) to maintain the divergence-free evolution of the magnetic field. LL-MHD is also installed in the AMR code ENZO, and has been used to study a range of astrophysical phenomena, from galaxy clusters (Xu et al. 2010) to pre-stellar cores (Collins et al. 2011).

3.5. PLUTO 3.1

The PLUTO code (Mignone 2009) is a highly modular, multidimensional and multi-geometry code that can be applied to relativistic or non-relativistic MHD or HD (hydrodynamic) flows. PLUTO comprises several numerical methods, such as the high-order conservative finite-difference divergence cleaning MHD method (Mignone & Tzeferacos 2010) as well as finite-volume CTU schemes (Mignone et al. 2010). The latest version of the PLUTO code (V. 3.1—2010 August) allows one to choose between several space reconstruction and time integration methods as well as several approximate Riemann solvers including HLL, HLLC, HLLD, or the Roe Riemann solver. For the MHD formulation one can choose between the eight-wave formulation (Powell et al. 1999), the divergence cleaning method (Dedner et al. 2002), and the CT method. The possibility of switching between several numerical methods allows one to handle a wide range of astrophysical problems. For this test we used the accurate Roe Riemann solver in combination with a third-order reconstruction (Čada & Torrilhon 2009), characteristic variable limiting, the Runge–Kutta 3 time integration, and the Powell et al. (1999) eight-wave MHD formalism; three-dimensional effects were incorporated by way of the Runge–Kutta integration without the use of the transverse flux gradients used in CTU. The Courant number was set to 0.3.

3.6. PPML

The piecewise parabolic method on a local stencil (PPML, Ustyugov et al. 2009) is a compact stencil variant of the popular PPM algorithm (Colella & Woodward 1984) for compressible magnetohydrodynamics. The principal difference between PPML and PPM is that cell interface states are evolved rather than reconstructed at every time step, resulting in a more compact stencil. The interface states are evolved using Riemann invariants containing all transverse derivative information. The conservation laws are updated in an unsplit fashion, making the scheme fully multidimensional. Divergence-free evolution of the magnetic field is maintained using the higher-order-accurate CT technique of Gardiner & Stone (2005). The method employs monotonicity constraints to preserve the order of scheme in points of local extrema (Suresh & Huynh 1997; Balsara & Shu 2000; Rider et al. 2007). To preserve monotonicity in multidimensions a method from Barth (1990) is additionally applied. An updated component of the electric field at a cell boundary is calculated by averaging the quantities obtained from known components of flux-vectors and values of gradient of the electric field (Gardiner & Stone 2005). The performance of PPML was tested on several numerical problems, which demonstrated its high accuracy on both smooth and discontinuous solutions (Ustyugov et al. 2009). Simulations of supersonic magnetized turbulence in three dimensions with PPML show that the low dissipation and wide spectral bandwidth of this method make it an ideal candidate for direct turbulence simulations (Kritsuk et al. 2009a, 2009b).

3.7. RAMSES

RAMSES (Teyssier 2002) is an unsplit Godunov AMR scheme with a second-order total variation diminishing spatial reconstruction using the Monotonized Central slope limiter. The magnetic field is updated using the CT method, using a two-dimensional Riemann problem at cell edges to compute the electro-motive force that enters into the induction equation. The magnetic field divergence, expressed in an integral form on cell

faces, is therefore zero down to machine accuracy. Conservative variables are updated by solving one-dimensional Riemann problems at cell faces. Both the one-dimensional and the two-dimensional Riemann solvers are based on the HLLD MHD approximate Riemann solution (Miyoshi & Kusano 2005). More details on the MHD scheme can be found in Teyssier et al. (2006) and Fromang et al. (2006).

3.8. STAGGER

The STAGGER Code is originally based on a code developed as part of the PhD thesis of Klaus Galsgaard (Galsgaard 1996). Several versions exist, and the code is used in many different circumstances (Galsgaard & Nordlund 1996; Padoan et al. 1997, 1998, 2000; Stein & Nordlund 1998; Asplund et al. 2000; Padoan et al. 2004; Gudiksen & Nordlund 2005; Braithwaite & Nordlund 2006; Archontis et al. 2007; Lunttila et al. 2009; Stein et al. 2011; Padoan & Nordlund 2011).

In the context of solar and stellar physics it is equipped with a multi-frequency radiative transfer module and a comprehensive equation of state module that includes a large number of atomic and molecular species, to be able to compute realistic three-dimensional models of the near-surface layers of stars. The widths, shifts, and asymmetries of synthetic spectral lines computed from such models exemplifies some of the most precise agreements between three-dimensional numerical simulations and astrophysical observations (Asplund et al. 2000).

In the context of supersonic turbulence studies earlier works (Padoan et al. 1997, 1998, 2000) were based on a non-conservative version of the code, which evolved the primitive variables $\ln \rho$, $\mathbf{u}$, and $\mathbf{B}$. The "per-unit-mass" formulation based on these variables is simple and robust, but has the disadvantage that mass and momentum are not conserved exactly by the discretized equations.

The current version of the code instead uses the per-volume variables ρ, $\rho\mathbf{u}$, and ρE, where E is the internal energy per unit mass, allowing a discretization that explicitly conserves mass, momentum, energy, and magnetic flux. In the isothermal case of relevance here the code solves these equations:

$$\frac{\partial \rho}{\partial t} = -\nabla \cdot \rho \mathbf{u}, \tag{4}$$

$$\frac{\partial \rho \mathbf{u}}{\partial t} = -\nabla \cdot (\rho \mathbf{u}\mathbf{u} + \underline{\tau}) - \nabla p + (\nabla \times \mathbf{B}) \times \mathbf{B}, \tag{5}$$

$$\frac{\partial \mathbf{B}}{\partial t} = -\nabla \times (-\mathbf{u} \times \mathbf{B} + \eta \nabla \times \mathbf{B}), \tag{6}$$

where $\underline{\tau}$ is the viscous stress tensor, which we write as

$$\tau_{ij} = -\rho \nu S_{ij}, \tag{7}$$

and S_{ij} is the strain rate

$$S_{ij} = \frac{1}{2}\left(\frac{\partial u_j}{\partial r_i} + \frac{\partial u_i}{\partial r_j}\right). \tag{8}$$

The viscosity ν and magnetic diffusivity η are spatially dependent, in a manner reminiscent of the Richtmyer & Morton formulation, with

$$\nu = (n_1 u_{\rm w} + n_2\, \delta u^+)\Delta s\,, \tag{9}$$

where Δs is the mesh size, $u_{\rm w}$ is the wave speed, δu^+ is the positive part of a second-order approximation of $-\Delta s\, \nabla \cdot \mathbf{u}$. The magnetic diffusivity is taken to be

$$\eta = n_B (n_1 u_{\rm w} + n_2 \delta u_B^+)\Delta s\,, \tag{10}$$

where δu_B^+ is analogous to δu^+, except only the component of the velocity perpendicular to $\mathbf{B}$ is counted.

Here, n_1, n_2, and n_B are numerical coefficients of the order of unity. The $n_1 u_{\rm w}$ term, where $n_1 \sim 0.03$ is a relatively small constant, is needed to provide stabilization and a weak dispersion of linear waves, while the $n_2\, \delta u^+$ term, with $n_2 \sim 0.5$, provides enhanced dissipation in shocks, where the rate of convergence $-\nabla \cdot \mathbf{u}$ is large. Since the magnetic field is insensitive to motions parallel to the field, only perpendicular motions are gauged by the corresponding magnetic diffusivity term. n_B is essentially an inverse magnetic Prandtl number.

The tensor formulation of the viscosity ensures that the viscous force is insensitive to the coordinate system orientation, thereby avoiding artificial grid-alignment.

3.9. ZEUS-MP

ZEUS-MP is a widely used, multiphysics, massively parallel, message-passing Eulerian code for astrophysical fluid dynamic simulations in three dimensions. ZEUS-MP is a distributed memory version of the shared-memory code ZEUS-3D that uses block domain decomposition to achieve scalable parallelism. The code includes hydrodynamics, magnetohydrodynamics, and self-gravity. The HD and MHD algorithms are based on the method of finite differences on a staggered mesh (Stone & Norman 1992a, 1992b), which incorporates a second-order-accurate, monotonic advection scheme (van Leer 1977). The MHD algorithm is suited for multidimensional flows using the method of characteristics scheme first suggested by Hawley & Stone (1995). Advection is performed in a series of directional sweeps that are cyclically permuted at each time step. Because ZEUS-MP is designed for large simulations on parallel computing platforms, considerable attention is paid to the parallel performance characteristics of each module in the code. Complete discussion on all algorithms in ZEUS-MP can be found in Hayes et al. (2006). All the MHD turbulence decay simulations performed using ZEUS-MP in this paper use a quadratic (von Neumann-Richtmyer) artificial viscosity coefficient qcon of 2.0 and a Courant number of 0.5.

4. DATA ANALYSIS

4.1. Power Spectra

Given a vector field $\mathbf{u}(\mathbf{r})$ discretized on a mesh i, j, k with $\mathbf{u}_{i,j,k}$ one can compute a power spectrum from the three-dimensional Fourier transform $\tilde{\mathbf{u}}_{i,j,k}$ by summing the magnitudes squared, $|\tilde{\mathbf{u}}_{i,j,k}|^2$, over k-shells with $K_n \leqslant |\mathbf{k}_{i,j,k}| < K_{n+1}$. If the Fourier transform coefficients $\tilde{\mathbf{u}}_{i,j,k}$ are normalized so the rms value of the corresponding function in real space is equal to unity, then the sum of the squares in Fourier space is equal to the average of the function squared in real space (Parseval's relation):

$$\mathrm{rms}^2 = \sum_{i,j,k} |\tilde{\mathbf{u}}_{i,j,k}|^2 = \frac{1}{N}\sum_{i,j,k} |\mathbf{u}_{i,j,k}|^2, \tag{11}$$

where N is the total number of i, j, k points.

In the codes used to analyze the results for the current paper we use the real valued Fast Fourier Transform routine `srfftf` from the `fftpack` software package, which returns coefficients $a_k = N/2$ for sine and cosine functions, except for the DC and Nyquist components, which return coefficients N. Proper power normalization requires that sine and cosine components contribute power 1/2, and the returned coefficients should thus be multiplied by $\sqrt{2}/N$, except for the DC and Nyquist components (which are the first and last coefficients returned from `srfftf`), which should be multiplied by $1/N$.

The power spectrum $P(k)$ expresses how much of the power falls in each k-interval. If the power is collected in discrete bins,

$$P_n = \sum_{K_n \leqslant |\mathbf{k}_{i,j,k}| < K_{n+1}} |\tilde{\mathbf{u}}_{i,j,k}|^2, \tag{12}$$

then the total power can also be expressed as

$$\mathrm{rms}^2 = \sum_n P_n, \tag{13}$$

where the sum is taken over all bins.

To illustrate the power spectrum P_n graphically one needs to assign a wavenumber k_n to each bin. A natural but not quite optimal choice is to use the midpoint of the bin; $k_n = (K_n + K_{n+1})/2$. A better choice is to use the mean of the wavenumbers that actually fall inside the bin (to see why this is better, consider a case with very wide bins and a function with power at only a few discrete wavenumbers).

It turns out that one gets smoother power spectra if one assigns a value

$$P'_n = \frac{4\pi}{3}\left(K_{n+1}^3 - K_n^3\right)\frac{1}{N_{\mathrm{bin}}}\sum_{\mathrm{bin}} |\tilde{\mathbf{u}}_{i,j,k}|^2 \tag{14}$$

rather than

$$P_n = \sum_{\mathrm{bin}} |\tilde{\mathbf{u}}_{i,j,k}|^2 \tag{15}$$

to each bin. In other words: power spectra (at least those measuring fluid flow properties) become smoother if they measure the *average power* in a shell (times the shell volume) rather than the total power. One can interpret this to mean that fluid flow properties are encoded in Fourier amplitudes as a function of wavenumber, rather than in total power of Fourier amplitudes in a shell. If (and only if) this is the case, then the power spectrum fluctuates (as observed) down (or up) if by chance a shell contains fewer (or more) discrete wavenumbers than expected.

To be able to recover P_n from P'_n (e.g., for use in Parseval's relation) it is necessary to record the number of discrete Fourier amplitudes in each bin, N_{bin} in Equation (14) above.

Note also, that in order for Parseval's relation to be exact for three-dimensional power spectra, all Fourier components need to be included, which means that the k-scale should really extend to a maximum value of $\sqrt{3}\,k_{\mathrm{N}}$, where k_{N} is the one-dimensional Nyquist frequency. Nevertheless, here we follow the common practice to truncate the three-dimensional power spectra at k_{N}.

4.2. Helmholtz Projections

The divergence of a vector field $\mathbf{f}_{i,j,k}$, with Fourier transform coefficients $\tilde{\mathbf{f}}_{i,j,k}$, is

$$\mathrm{FT}(\nabla \cdot \mathbf{f}) = i\mathbf{k}_{i,j,k} \cdot \tilde{\mathbf{f}}_{i,j,k}. \tag{16}$$

The vector coefficients $\tilde{\mathbf{f}}_{i,j,k}$ may be split into a component parallel to $\mathbf{k}_{i,j,k}$ and a remaining component, which is perpendicular to $\mathbf{k}_{i,j,k}$:

$$\tilde{\mathbf{f}}^{\parallel}_{i,j,k} = \mathbf{k}_{i,j,k}(\mathbf{k}_{i,j,k} \cdot \tilde{\mathbf{f}}_{i,j,k})/|\mathbf{k}_{i,j,k}|^2, \tag{17}$$

and

$$\tilde{\mathbf{f}}^{\perp}_{i,j,k} = \tilde{\mathbf{f}}_{i,j,k} - \tilde{\mathbf{f}}^{\parallel}_{i,j,k}. \tag{18}$$

Taking the divergence of the latter, we have

$$i\mathbf{k}_{i,j,k} \cdot \tilde{\mathbf{f}}^{\perp}_{i,j,k} = i\mathbf{k}_{i,j,k} \cdot \tilde{\mathbf{f}}_{i,j,k} - i\mathbf{k}_{i,j,k} \cdot \mathbf{k}_{i,j,k}(\mathbf{k}_{i,j,k} \cdot \tilde{\mathbf{f}}_{i,j,k})/|\mathbf{k}_{i,j,k}|^2 = 0. \tag{19}$$

The inverse transform based on the $\tilde{\mathbf{f}}^{\perp}_{i,j,k}$ coefficients is thus solenoidal, while the inverse transform based on $\tilde{\mathbf{f}}^{\parallel}_{i,j,k}$ is purely compressional.

5. RESULTS

There is a great variety of interesting statistical measures in magnetized supersonic turbulent flows to study and compare. The KITP07 project originally implied a comparison of density structures in physical space using projections and slices, PDFs of the gas density, various power spectra and structure functions, time evolution of some global and local average quantities, etc. Most of these data provided by individual contributors to the project can be accessed electronically via the wiki Web site at KITP under the rubric *Star Formation Test Problems*.[18]

In this paper, we mainly focus on the statistics of the basic MHD fields (the so-called primitive variables) since those are easier to interpret and link back to the essential features of the numerical methods. Since the system of equations and the initial and boundary conditions are the same for all codes, the only source of differences in the numerical solutions is numerical dissipation. In this section, we discuss the sensitivity of various turbulence diagnostics to the numerics and describe a set of statistical measures that allow us to assess the quality of different algorithms we compare. We begin with global averages over the periodic domain and then continue with analysis of power spectra. We avoid discussion of density statistics, even though these are important for numerical star formation studies. That discussion would be more appropriate in a context of driven turbulence, where time-averages over many flow snapshots help to reduce the strong statistical noise associated with the density (e.g., Kritsuk et al. 2006, 2007). The density statistics in a similar context have been discussed in detail elsewhere (e.g., Kitsionas et al. 2009; Price & Federrath 2010).

5.1. Mean Kinetic and Magnetic Energy, rms Mach Numbers

The evolution of the mean kinetic energy is captured perfectly well by all methods, except for some small (<8% by $t = 0.2$, see Table 1) differences that become noticeable at $t > 0.12$ in Figure 1. This particular quantity is known to converge rather early in nonmagnetized compressible turbulence simulations, and the same is true for super-Alfvénic turbulence (Lemaster & Stone 2009; Kritsuk et al. 2009b). The velocity power spectrum $P(\mathbf{u}, k) \sim k^{\alpha}$ has an inertial range slope $\alpha \in [-2, -5/3]$ that depends on the sonic Mach number (see, for instance, Figure 3 below). Because the spectral slope is so steep, the mean specific kinetic energy density, $E_{\mathrm{K}} \equiv \langle \mathbf{u}^2/2 \rangle = \int_0^{\infty} P(\mathbf{u}, k)dk/2$, is strongly dominated by large scales. If the resolution is sufficient

[18] http://kitpstarformation07.wikispaces.com/Star+Formation+Test+Problems

Table 1
Selected Numeric Values for the Decay Test

Code	$E_K/E_{K,ref}$[a]	$E_M/E_{M,ref}$[b]	$2\Omega + 4/3\Delta$[c]	J^2[d]	**u**-bandwidth[e]	**B**-bandwidth[f]	$\bar{\chi}(k > 100k_{min})$[g]
ENZO	1.001	0.78	0.93	0.92	0.19	0.07	0.60
FLASH	1.000	0.94	0.85	1.38	0.15	0.20	0.27
KT-MHD	1.041	0.85	0.89	1.30	0.20	0.13	0.86
LL-MHD	1.062	0.81	1.02	0.80	0.22	0.10	0.29
PLUTO	1.077	0.92	1.03	1.14	0.20	0.12	0.32
PPML	1.043	0.92	1.20	1.46	0.24	0.20	0.32
RAMSES	1.069	0.87	1.07	1.18	0.24	0.09	0.33
STAGGER	1.005	0.70	1.93	0.79	0.28	0.07	0.31
ZEUS	1.037	0.83	0.76	1.01	0.16	0.10	0.27

Notes.
[a] Mean specific kinetic energy density at $t = 0.2$ normalized by the reference solution; see Section 5.1 and Figure 1.
[b] Mean magnetic energy density at $t = 0.2$ normalized by the reference solution; see Section 5.1 and Figure 1.
[c] A proxy for the mean dissipation rate of specific kinetic energy at $t = 0.02$; see Section 5.2 and Figure 2, left.
[d] A proxy for the mean dissipation rate of magnetic energy at $t = 0.02$; see Section 5.2 and Figure 2, right.
[e] Effective spectral bandwidth for the velocity; see Section 5.4 and Figure 4, left.
[f] Effective spectral bandwidth for the magnetic field; see Section 5.4 and Figure 4, right.
[g] Ratio of dilatational-to-solenoidal power averaged over $k/k_{min} > 100$ at $t = 0.2$; see Section 5.5 and Figure 5, right.

to properly capture the structure of large-scale flow in the computational domain, the energy convergence is achieved. This is apparently the case in our 512^3 simulations; see the left panels of Figure 1. For the 256^3 model (not shown), the result is very similar. We thus conclude that in the decaying turbulence problem the mean kinetic energy is not sensitive to variations in small-scale numerical diffusivity between different methods.

The mean magnetic energy density, $E_M \equiv \langle \mathbf{B}^2/2 \rangle = \int_0^\infty P(\mathbf{B}, k)\, dk/2$, appears to be more sensitive to variations in small-scale numerical kinetic and magnetic diffusivity in super-Alfvénic simulations; see Figure 1, right panels, and Table 1. Most of the methods show an early-time increase in magnetic energy, but asymptotically, after saturation is reached, all of them show very similar decay rates $\dot{E}_M/E_M$. The saturated level of E_M in the initial flow snapshot generated with the original, non-conservative version of the STAGGER code is lower than most other codes would produce, except for perhaps LL-MHD and ENZO. To compensate for this deficiency of magnetic energy in the initial conditions, FLASH and PPML add about 7% to the initial E_M by the time $t_1 = 0.02$, when the first flow snapshot is recorded. KT-MHD increases E_M by ∼4%, PLUTO, ZEUS and RAMSES add ∼1%–2%. The level of E_M reached with the old STAGGER code is roughly consistent with that of ENZO and LL-MHD. The new, conservative STAGGER appears to be more diffusive than all other methods as far as the magnetic energy density is concerned.

To understand why the magnetic energy levels are different, one needs to recall that the convergence rate for E_M with the grid resolution is rather slow at 512^3. For instance, with PPML, the saturated levels of E_M in driven simulations continuously grow as grid resolution improves and the convergence is expected only at 2048^3 or even higher (Kritsuk et al. 2009b; Jones et al. 2011).[19] The slow convergence of E_M in super-Alfvénic runs is not surprising because of their rather shallow magnetic energy spectra (see Figure 3 below and note that the magnetic spectra are plotted noncompensated). In such weakly magnetized ($B_0 \ll b_{rms}$) isotropic nonhelical flows, turbulence amplifies the rms magnetic field fluctuations by stretching and tangling the field lines primarily on small scales until an equilibrium is reached between the rms field amplification and dissipation. The saturated level of E_M for a given sonic Mach number, M_s, and mean magnetic field strength, B_0, would naturally depend on the effective magnetic Prandtl number and on the effective magnetic Reynolds number. We discuss the relative standing of the methods in terms of Rm and Pm in the next section and show that the saturation level of magnetic energy indeed correlates with Rm and Pm. Overall, by $t = 0.2$, the deviations of E_M from the reference solution defined in Section 5.4 can be as large as 30%, see Table 1.

Turbulence regimes simulated with different methods differ slightly in their rms Alfvénic Mach numbers, $M_A = \sqrt{2\langle \rho u^2 \rangle / \langle B^2 \rangle}$. We use this proxy for the Alfvénic Mach number instead of $\sqrt{2\langle \rho u^2/B^2 \rangle}$ since in the latter case the locations where B (nearly) vanishes would produce arbitrarily large contributions to the mean making this measure unstable.

At $t = 0.1$, the least super-Alfvénic regime is achieved with FLASH and PPML, followed by PLUTO, KT-MHD, RAMSES, ZEUS, ENZO, LL-MHD, and the new STAGGER code in order of increasing M_A. Note that the ranking of the methods is essentially the same as for E_M, which, unlike M_A, does not depend on the gas density. This similarity can be explained by a limited sensitivity of our chosen proxy for M_A to correlations between density and velocity or between density and field strength (Kritsuk et al. 2009a).

Finally note that while E_K decays by a factor >10 during the course of the simulation, the decay of E_M proceeds much slower, only by a factor of ∼2. Similar to the incompressible case (Biskamp 2003), in supersonic turbulence the energy ratio $\Gamma \equiv E_K/E_M$ is not constant but decreases with time. While M_s decreases by a factor of ∼3 from ∼9 to ∼2.6, M_A shows a 2.5× drop from ∼4.5 to ∼1.8. These differences in the decay rates of kinetic and magnetic energy as well as in the behavior of M_s and M_A can be understood as consequences of self-organization, i.e., the relaxation of the turbulence towards an asymptotic static force-free minimum-energy state (e.g., Biskamp 2003).

[19] Note that, strictly speaking, the ILES approach involved here does not imply convergence as grid resolution improves since the effective Reynolds number is ultimately a function of the grid size (e.g., Kritsuk et al. 2006). At the same time, an asymptotic regime corresponding to $\mathrm{Re} = \infty$ can potentially be reached relatively early, at large, but still finite Reynolds numbers. This is what we probably observe as grid resolution approaches 2048^3 in super-Alfvénic simulations.

5.2. Small-scale Kinetic and Magnetic Diagnostics

Another way to look at the effects of numerical dissipation is to analyze the time evolution of enstrophy $\Omega = \frac{1}{2}\langle|\nabla \times \mathbf{u}|^2\rangle$, dilatation $\Delta = \langle|\nabla \cdot \mathbf{u}|^2\rangle$, and that of the mean squared current density $J^2 = \langle|\nabla \times \mathbf{B}|^2\rangle$. These so-called "small-scale" quantities show strong oscillations at the grid scale. Their spectra are dominated by the high wavenumbers, and their PDFs have extended exponential tails (e.g., Porter et al. 2002). They also usually display a very slow (if any) convergence with grid resolution in ILESs due to a strong dependence on Re and Rm. These measures are related to the total viscous and Ohmic dissipation rates within the periodic domain (e.g., Kritsuk et al. 2007). For instance, in nonmagnetized compressible turbulence, which is in many respects similar to the super-Alfvénic case considered here, the mean dissipation rate of the specific kinetic energy can be expressed as $\epsilon_K = -(\mathrm{Re})^{-1}(2\Omega + 4/3\Delta)$ (e.g., Pan et al. 2009).[20] Since the global dissipation rates for E_K are very similar for all the methods considered here (see Figure 1), the relative ranking of their effective Reynolds numbers is fully determined by the value of $2\Omega + 4/3\Delta$. We can thus use the dissipation rates plotted in the left panel of Figure 2 to determine the relative standing of these methods in terms of their $\mathrm{Re}_{\mathrm{eff}}$. The new STAGGER code shows an outstanding result during the first half of the evolution, $t \in [0, 0.1]$, when its $\mathrm{Re}_{\mathrm{eff}}$ exceeds that of PPML by up to a factor of ∼1.5. RAMSES, PLUTO, LL-MHD, ENZO, KT-MHD, FLASH, and ZEUS follow STAGGER and PPML in order of decreasing effective Reynolds number. See Table 1 for numeric values of $2\Omega + 4/3\Delta$ from different codes at $t = 0.02$.

We employ the same approach to get an assessment of the relative standing of these numerical methods in terms of their effective magnetic Reynolds number, $\mathrm{Rm}_{\mathrm{eff}}$. Figure 2, right panel shows the mean-squared current density, J^2, as a function of time. The current density is sensitive to both ϵ_M and $\mathrm{Rm}_{\mathrm{eff}}$, since $\epsilon_M \sim -(\mathrm{Rm})^{-1} J^2$. We expect qualitatively the same dependency here as for ϵ_K and $\mathrm{Re}_{\mathrm{eff}}$, but with, perhaps, different orders of the methods. Note, however, that the dissipation rates and saturated levels of magnetic energy are not the same for different methods as can be seen in Figure 1, right panel. PPML shows the highest $\mathrm{Rm}_{\mathrm{eff}}$, followed by FLASH, KT-MHD, RAMSES, PLUTO, ZEUS, ENZO, LL-MHD, and STAGGER. Note that the order in which the methods follow each other in the right panel of Figure 2 is the same as in the E_M plot in Figure 1; see also Table 1. Thus, $\mathrm{Rm}_{\mathrm{eff}}$ and E_M are positively correlated. We will explore this correlation further in Sections 5.3 and 5.4, where we analyze the power spectra of kinetic and magnetic energy and measure the effective bandwidth of the methods.

5.3. Power Spectra

Figure 3 shows power spectra of the velocity and magnetic energy at $t = 0.02$, 0.06, and 0.2. The spectra obtained at 512^3 demonstrate a very good agreement with each other up to $\log_{10} k/k_{\mathrm{min}} \sim 1.2$ and slightly diverge at higher wavenumbers. This means that numerical dissipation strongly affects the scales smaller or equal to ∼16 grid cells in supersonic turbulence simulations with our best methods.

The new STAGGER code shows a very extended spectrum at $t = 0.02$ with an asymptotic slope of $-5/3$ up to $\log_{10} k/k_{\mathrm{min}} \lesssim 2$. This slope is not preserved, however, for the whole duration of the simulation. By $t = 0.2$, when after many integration time steps the sonic Mach number drops to ∼2.5, the spectrum looses some high-k power and progressively bends down at $\log_{10} k/k_{\mathrm{min}} \gtrsim 1.5$ leaving behind PLUTO, RAMSES, PPML, and LL-MHD. A close inspection of the velocity spectra shows that numerical diffusion in ZEUS, FLASH, KT-MHD, and ENZO is somewhat stronger than in the rest of the grid-based codes and affects the velocities at lower wavenumbers. Besides the new STAGGER code, RAMSES, PLUTO, PPML, and LL-MHD are the least diffusive codes. The magnetic energy spectra display similar variations, but the ranking of methods is different. Here FLASH and PPML show very low magnetic diffusivity, while RAMSES, ZEUS, STAGGER, LL-MHD, and ENZO are more diffusive and KT-MHD stays in between.

5.4. Effective Spectral Bandwidth

In order to highlight variations in the power spectra obtained with different methods, we follow the procedure developed in Lele et al. (2009) and Johnsen et al. (2010) for compressible Navier–Stokes turbulence at moderate Mach numbers. We have seen that PPML is one of the least diffusive methods here, so we declare the 1024^3 PPML solution filtered with a low-pass Gaussian filter down to 256^3 to be "exact" and call it the *reference solution*. We then plot power spectra compensated by the spectrum of this reference solution for the first snapshot at $t = 0.02$, see Figure 4. We set tolerance at a level of ±25% from the reference solution and define the spectral bandwidth of a method as the fraction of the Nyquist frequency where the compensated spectrum deviates by more than 25% from the reference solution. While this definition is rather arbitrary, it helps to establish a convenient quantitative measure to assert the performance of numerical methods for the turbulence decay test, see Table 1 for numeric values.

The left panel of Figure 4 shows the compensated velocity spectra. STAGGER, PPML, and RAMSES have the highest spectral bandwidth in velocity. The second position is shared by LL-MHD, PLUTO, KT-MHD, and ENZO. ZEUS and FLASH show a similar velocity bandwidth. RAMSES and KT-MHD show a small bump at $\log_{10} k/k_{\mathrm{min}} \in [0.6, 1.1]$ reminiscent of the bottleneck effect, while the STAGGER and PPML spectra decrease monotonically.

The right panel of Figure 4 shows the compensated magnetic energy spectra. The situation here is quite different. First, unlike the velocity spectra, the magnetic energy spectra start to bend down from the reference solution rather early. This is expected because of the slow convergence of E_M with grid resolution, as we discussed earlier. FLASH and PPML demonstrate the highest bandwidth, KT-MHD is in the middle, PLUTO, ZEUS, LL-MHD, ENZO, and RAMSES are very similar to each other and show a somewhat higher magnetic diffusivity. At 256^3, the spectral bandwidth of our best MHD codes is ∼0.3 for the velocities and ∼0.2 for the magnetic energy. If we were dealing with properly converged solutions obtained from a direct numerical simulation as in Johnsen et al. (2010), that would mean that numerical dissipation strongly affects the wavenumbers down to at least $(0.2–0.3)k_N$. This is not however exactly the case here due to the adopted ILES approach, see footnote 17.

5.5. Dilatational versus Solenoidal Modes

We have discussed above how the numerical methods differ in their kinetic and magnetic diffusivity. This aspect plays an

[20] Strictly speaking, this is only valid for compressible Navier–Stokes turbulence assuming zero bulk viscosity, i.e., for ideal monoatomic gases.

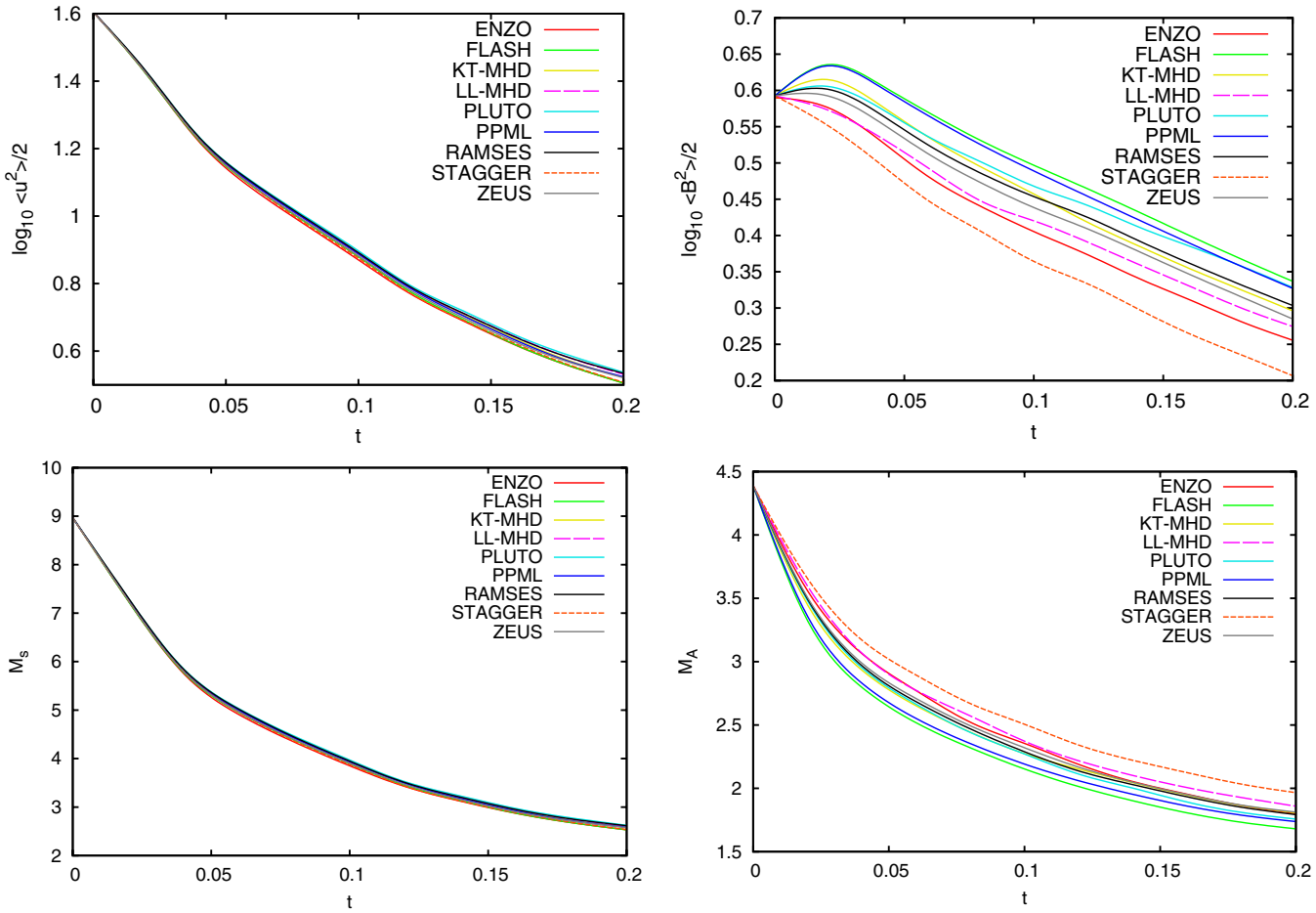

Figure 1. Time evolution of the mean specific kinetic energy (top left), magnetic energy (top right), and sonic (bottom left) and Alfvénic (bottom right) rms Mach numbers at a grid resolution of 512^3 cells. Note that the kinetic energy and sonic Mach number are rather insensitive to the details of numerical dissipation while the evolution of magnetic energy and Alfvénic Mach number display significant dependence on the numerical magnetic diffusivity.

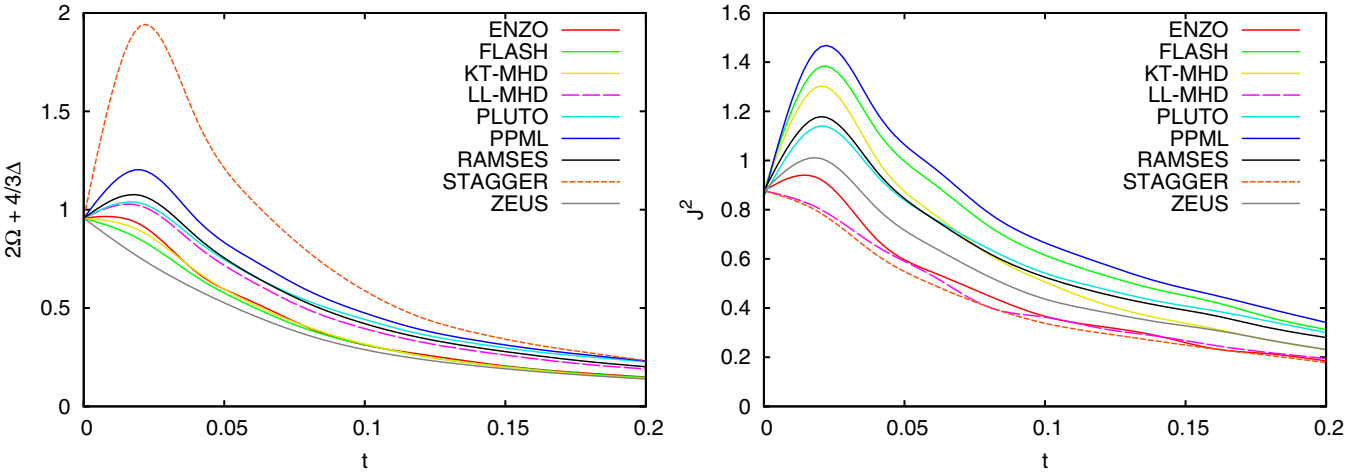

Figure 2. Time evolution of $-\epsilon_K \mathrm{Re}_{\mathrm{eff}} = 2\Omega + 4/3\Delta$ defined in Section 5.2 (left) and the mean-squared current, $J^2 = \langle|\nabla \times \mathbf{B}|^2\rangle$ (right). These "small-scale" measures of turbulent fluctuations are sensitive to the details of numerical diffusivity and highlight differences between the methods.

important role in simulations involving small-scale turbulent dynamo. There Pm serves as a control parameter and the dynamo would only operate at $\mathrm{Pm} > \mathrm{Pm}_{\mathrm{crit}}$ (Brandenburg & Nordlund 2011).

In this section, we look at how different methods treat dilatational and solenoidal components of the velocity field on small scales. We decompose the velocity fields into the potential (curl-free) and rotational (solenoidal) components, $\mathbf{u} = \mathbf{u}_{\mathrm{d}} + \mathbf{u}_{\mathrm{s}}$,

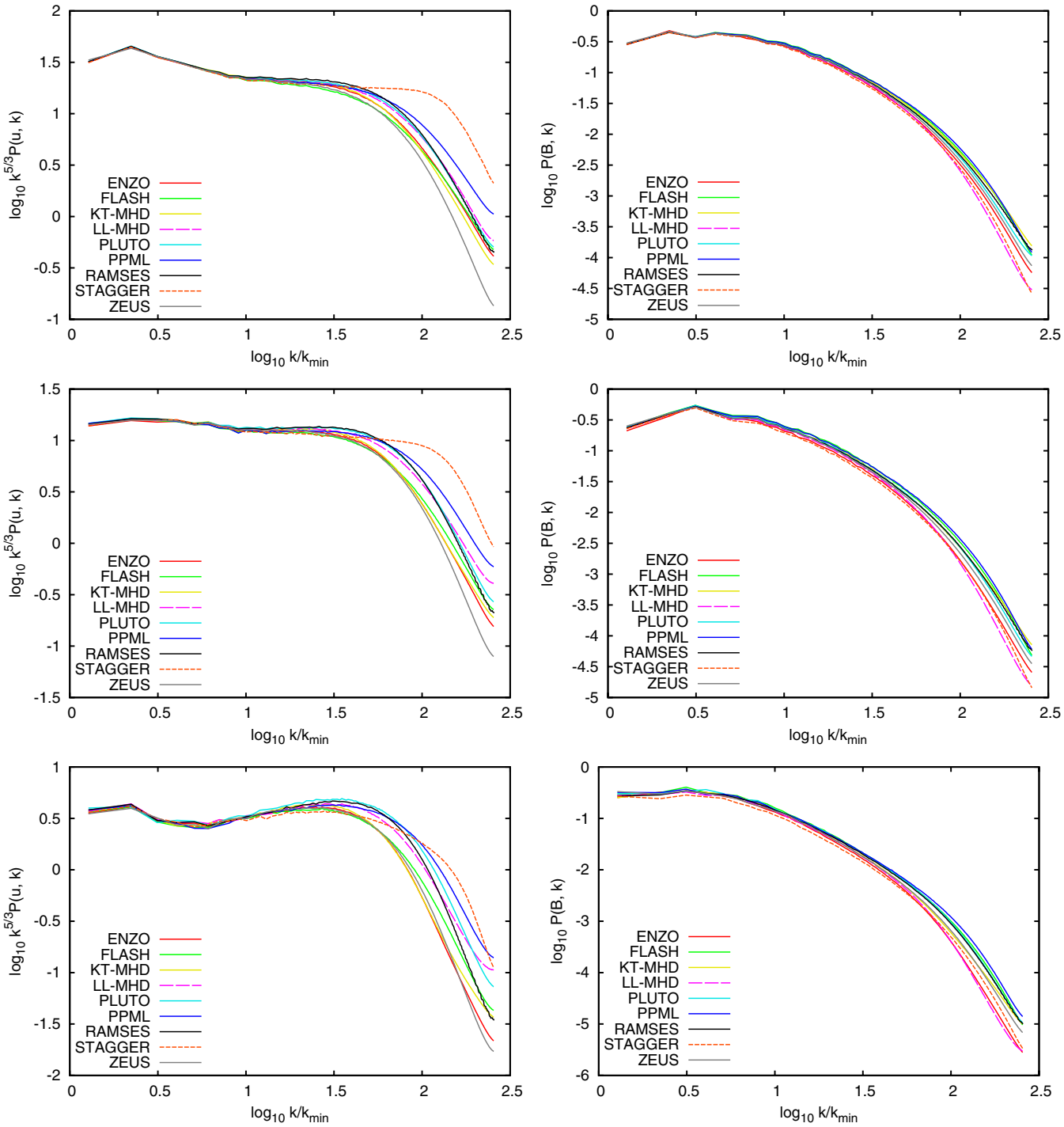

Figure 3. Power spectra of the velocity (left panels) and magnetic energy (right panels) on a 512^3 grid for flow snapshots 1, 3, and 10 at $t = 0.02$, 0.06, and 0.2 (top-to-bottom), respectively. The velocity spectra are compensated with $k^{5/3}$, while there is no compensation for the magnetic energy spectra. Note that the ordinate scale is not always the same for different time instances.

using Helmholtz decomposition. We compute power spectra, $P(\mathbf{u}_\mathrm{d}, k)$ and $P(\mathbf{u}_\mathrm{s}, k)$, and define the dilatational-to-solenoidal ratio as $\chi(k) \equiv P(\mathbf{u}_\mathrm{d}, k)/P(\mathbf{u}_\mathrm{s}, k)$. Peculiarities in the small-scale $\chi(k)$ ratio have a potential to affect various turbulence statistics (e.g., the density PDF) and limit (or even eliminate) the extent of the inertial range in simulations. These features cannot be captured by either the small-scale kinetic diagnostics discussed in Section 5.2 or by the power spectra discussed in Section 5.3. We present $\chi(k)$ for snapshots 1 and 10 ($t = 0.02$ and 0.2) in the left and right panels of Figure 5, respectively. Table 1 gives numeric values for the average dilatational-to-solenoidal ratio, $\bar{\chi}(k/k_\mathrm{min} > 100)$, at wavenumbers above $100k_\mathrm{min}$ in the 512^3 models at $t = 0.2$.

First, note a very good agreement between all the methods in the early snapshot at low wavenumbers, $\log_{10} k/k_\mathrm{min} < 1.3$, with $\chi(k/k_\mathrm{min} = 10) \approx 0.47$. An overall ratio of 1:2 is expected for super-Alfvénic turbulence at high Mach numbers (Kritsuk et al. 2010; Federrath et al. 2010). As the turbulence decays, the sonic Mach number drops down to $M_\mathrm{s} \sim 2.7$ by $t = 0.2$ and the ratio decreases to $\chi(k/k_\mathrm{min} = 10) \approx 0.33$, as

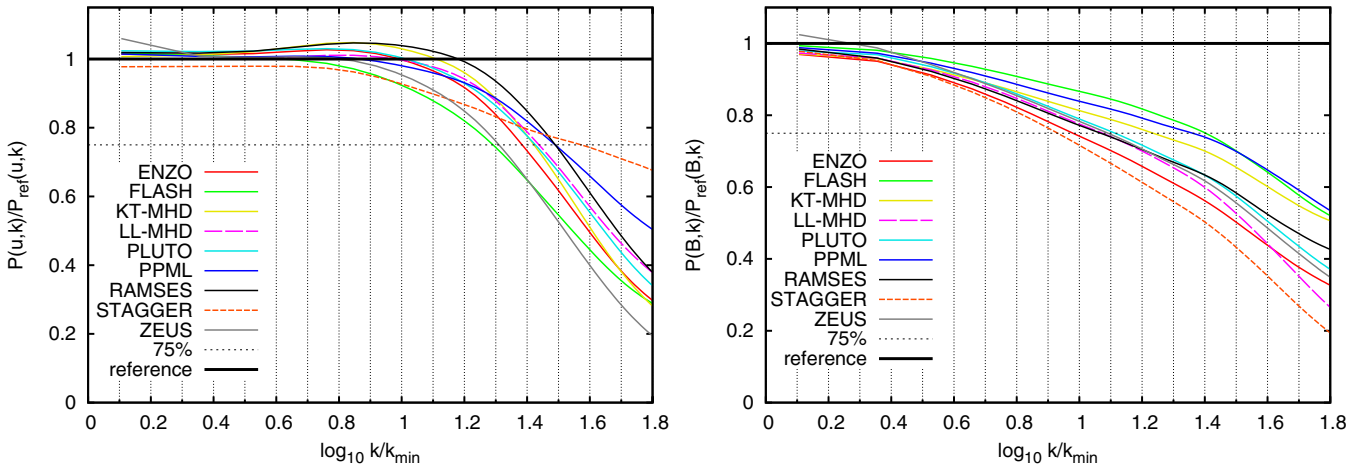

Figure 4. Compensated power spectra of the velocity (left panel) and magnetic energy (right panel) for the first flow snapshot at $t = 0.02$ from the 256^3 simulations.

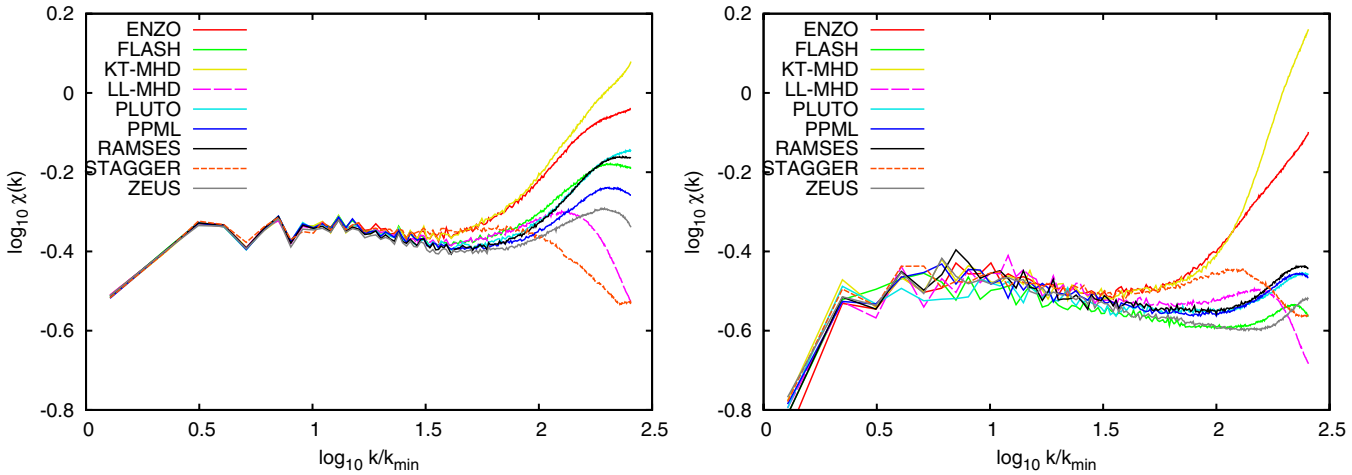

Figure 5. Ratio of dilatational-to-solenoidal power in velocity spectra, $\chi(k)$, for the first (left panel) and the last (right panel) flow snapshots from the 512^3 simulations at $t_1 = 0.02$ and $t_{10} = 0.2$, respectively.

expected. In the inertial range, $\chi(k)$ is known to be a slowly decreasing function of the wavenumber (Kritsuk et al. 2007, 2010) and this behavior is nicely captured by most of the codes. There are slight differences in the $\chi(k)$ levels between different methods at $t = 0.2$ with ZEUS and FLASH being slightly ahead of the other codes in damping the dilatational modes at high wavenumbers. Otherwise, the results from different methods look very similar, although ENZO, KT-MHD, and STAGGER start to deviate somewhat from the rest of the codes at relatively low wavenumbers, $\log_{10} k/k_{\rm min} \sim 1.5$. Also KT-MHD and ENZO produce unusually high χ values at the Nyquist wavenumber. For instance, KT-MHD has $\chi(k_{\rm N}) \approx 1.25$ and 1.5 at $t = 0.02$ and 0.2, respectively. This indicates that perhaps some spurious compressible fluctuations are present at scales $k \gtrsim k_{\rm N}/8$ in simulations carried out with these codes. The small-scale oscillations of the KT-MHD code are likely to be caused by the way the CT scheme is implemented (R. Kissmann 2010, private communication). The observed compressible artifacts can probably be reduced to a large extent by using the CT approach proposed by Londrillo & del Zanna (2004).

6. DISCUSSION

One is tempted to try to sort these nine methods into some well-ordered set. This is, however, an impossible task, as no single solver consistently outperformed all others on all diagnostics. In this discussion, we will restrict our focus to discussing kinematic and magnetic dissipation, as measured by the diagnostics presented here. This leaves out other potentially important diagnostics, such as the loop advection test of Gardiner & Stone (2005). We are also ignoring other salient features, such as computational cost (in memory and time to solution), ease or feasibility of extending the solver to different physical or numerical scenarios, or quality of documentation, all of which go into the selection of a code package. The final result is that all codes performed reasonably well on the task. There is no single silver bullet that determines the performance of a given solver; good quality results can be achieved through a variety of means, and dissipation can be introduced in a variety of places.

All MHD algorithms used in this work are extensions of a previously established hydrodynamic algorithm. In general, five basic features determine the operation of a numerical scheme, base method (most prominently spatial order of accuracy), MHD extension, artificial viscosity, time integration, and directional splitting. In this section, we will classify each code based on these parameters and discuss trends within each feature. In Section 6.1, we discuss the spatial order of accuracy, which seems to be the dominant factor in determining performance. In Section 6.2, we will discuss artificial viscosity and source

Table 2
Solver Design Specifications for the Eulerian Methods[a]

Name	Base Scheme[b]	Spatial Order[c]	Source Terms[d]	MHD[e]	Time Integration[f]	Directional Splitting[g]
ENZO	FV, HLL	Second	Dedner	Dedner	Second-order RK	Direct
FLASH	FV, HLLD	Second	$\parallel$ Derivative	Third-order CT	Forward Euler	$\perp$ Reconstruction
KT-MHD	FD, CWENO	Third	KT	Third-order CT	Fourth-order RK	Direct
LL-MHD	FV, HLLD	Second	None	Athena CT	Forward Euler	Split
PLUTO	FV, HLLD	Third	Powell	Powell	Fourth-order RK	Direct
PPML	FV, HLLD	Third	None	Athena CT	Forward Euler	$\perp$ Reconstruction
RAMSES	FV, HLLD	Second	None	2D HLLD CT	Forward Euler	$\perp$ Reconstruction
STAGGER	FD, Stagger	Sixth	Tensor	Staggered CT	Third-order Hyman	Direct
ZEUS	FD, van Leer	Second	von Neumann	MOC-CT	Forward Euler	Split

Notes.
[a] See Section 3 and the indicated sections on each topic for more information.
[b] Base method. FD for finite difference, FV for finite volume. FV techniques have the Riemann solver listed, Section 6.3.
[c] Spatial order of accuracy, Section 6.1.
[d] Artificial Viscosity, Section 6.2. "$\parallel$ Derivative" indicates presence of terms proportional to the longitudinal derivative of the magnetic field.
[e] MHD method, Section 6.4.
[f] Time integration method, Section 6.6.3.
[g] Multidimensional technique, Section 6.6.2. "$\perp$ Reconstruction" indicates presence of transverse derivatives in the interface reconstruction.

terms that behave as a viscosity. These features also seem to have considerable impact on the dissipation properties, as one would expect. In Section 6.3, we will classify and discuss other properties of the base hydrodynamical scheme. In Section 6.4, we will discuss the performance of various MHD extension methods. In Section 6.5, we will discuss three closely related schemes and discuss how seemingly small details can dramatically effect the results. In Section 6.6, we will discuss directional splitting, time integration, and reconstructed variables. These seem to have a less dramatic impact on the overall performance, as measured by the diagnostics. See Table 2 for a summary of these solver configuration details.

We refer the reader to the excellent books by Toro (1999), Laney (1998), and LeVeque (2002) and the method papers cited in Section 3 for the details of each numerical scheme. We will not be expanding on any details except where necessary.

6.1. Spatial Order of Accuracy

High spatial order of accuracy seems to be the salient feature of the least dissipative codes, though there are many factors in each method that can improve or degrade performance. STAGGER has the highest spatial order, 6, and this is reflected most notably in Figure 2, left panel, where its effective Reynolds number is significantly higher than the other methods, and Figure 3, left panel, where the inertial range of the power spectrum extends much further than the others. The third-order methods are PPML, PLUTO, KT-MHD, and the electric field construction of FLASH. These four methods show the highest magnetic spectral bandwidth, and are the top performers in the effective magnetic Reynolds number and magnetic power spectrum. However, other effects, most likely viscosity, keep these third-order methods from having the lowest dissipation among all statistics. The remaining methods (ZEUS, RAMSES, LL-MHD, ENZO, and the base hydro scheme of FLASH) are second order spatially. These codes tend to show more dissipation over the third-order methods.

There are two notable exceptions to this trend. The first can be seen in the spectral bandwidth plot, in which RAMSES (second order spatially) performs better than some third-order methods, though this may be due to other effects (see Section 6.5). The second exception can be seen in the top curve of the effective Reynolds number, corresponding to the STAGGER method. The initial conditions were generated with an early version of STAGGER, but continued with a version that used conservative variables and different settings for the artificial viscosity. As both methods are sixth order spatially, the increase in effective Reynolds number demonstrates that it is not spatial accuracy alone that determines dissipation properties. This will be discussed further in Section 6.2. Note that here we refer only to the formal spatial order of accuracy for the reconstruction or interpolation of each scheme. The actual convergence properties of each scheme, once time integration, spatial reconstruction, etc. have been taken into account, must be measured as a function of time and/or space resolution. This is beyond the scope of this work.

6.2. Artificial Viscosity and Source Terms

It is quite typical for numerical schemes to include some form of artificial viscosity in order to avoid numerical instabilities. In the case of the Powell et al. (1999) and Dedner et al. (2002) MHD schemes, source terms proportional to $\nabla \cdot \mathbf{B}$ are included to constrain the effects of divergence, which while not the same kind of dissipation still have a dissipative effect. In this suite of simulations, viscosity treatments can be broken coarsely into three categories: artificial viscosity, $\nabla \cdot \mathbf{B}$ motivated diffusivity, and exclusively numerical viscosity. Explicit terms are included in STAGGER, KT-MHD, ZEUS. Terms due to $\nabla \cdot \mathbf{B}$ treatments are included in PLUTO and ENZO. The four remaining codes have no explicit artificial viscosity, and dissipation is only due to the scheme itself (these are FLASH, PPML, RAMSES, and LL-MHD).

One naively expects that codes with explicit viscosity terms will have somewhat more dissipation than those without. However, this is only loosely seen in the results, and it is difficult to disentangle dissipative terms from other code differences. STAGGER gives the most noticeable example of the effects of dissipation, namely the large gap between its velocity dissipation, which is quite low, and its magnetic dissipation, which is quite a bit higher than other codes on most metrics. It is also possible that the fine tuning of the magnetic and kinematic artificial diffusivity, which has maximized the apparent inertial range, has altered the non-local coupling of MHD waves in a

manner that still leaves the dissipation relatively high in the inertial range. It is reasonable to isolate codes based on spatial order of accuracy in order to compare viscosity results. Among the third-order codes, PPML, with no explicit viscosity, tends to have lower dissipation than PLUTO, which has $\nabla \cdot \mathbf{B} = 0$ motivated source terms, which in turn tends to have lower dissipation than KT-MHD. Then isolating the second-order methods, the trend somewhat continues, though less robustly. ENZO and ZEUS tend to show the most velocity dissipation, as measured by the effective Reynolds number or velocity bandwidth. However, ENZO is the only second spatial order code with explicit magnetic dissipation, and it shows more power in the magnetic power spectrum than LL-MHD, which has none. RAMSES shows the lowest dissipation among the second-order codes in all metrics except for magnetic spectral bandwidth, in which ZEUS is slightly higher.

One method (FLASH) includes terms proportional to the longitudinal derivative of the magnetic field. These terms are typically omitted from the derivation as they are identically zero in the one-dimensional version of the equations.

6.3. Base Methods

Eulerian hydro schemes fall broadly into two categories: finite volume and finite difference. In loosest terms, finite-volume schemes approximate the integral form of the conservation law, while finite-difference terms approximate the differential form of the conservation law. Three of the grid-based codes compared here are finite difference: STAGGER, KT-MHD, and ZEUS. The other six are finite-volume methods (ENZO, FLASH, LL-MHD, PLUTO, PPML, and RAMSES.) Between finite volume and finite difference, there is no correlation with performance. This is best illustrated in the left panel of Figure 2. The code with the highest effective Reynolds number is STAGGER, and with the lowest is ZEUS, and both are finite-difference methods. Here we will discuss some common features within each category of methods.

6.3.1. Finite-difference Methods

One of the curses of numerical fluid dynamics is the battle between accuracy and stability. This seems to be felt somewhat more strongly by the three finite-difference codes. ZEUS tends to be more dissipative than other methods, even though it is formally second order spatially (see, for instance, the effective Reynolds number in Figure 2, left, or the left panels of Figure 3). STAGGER has the highest effective fluid Reynolds number, but the lowest effective magnetic Reynolds number; we believe this to be a result of the tensor viscosity and its subtle relationship to the (scalar) magnetic diffusivity. The KT-MHD method suffers from excessive small-scale compression, likely due to the fact that CWENO schemes are only *essentially* non-oscillatory, trading the possibility of small numerical oscillation near shocks for very high quality results in smooth regions.

6.3.2. Finite-volume Methods

The six finite-volume methods (ENZO, FLASH, LL-MHD, PLUTO, PPML, and RAMSES) are all some form of higher-order extension of Godunov's method. These methods have the advantage that they capture shock structures, in principle, exactly. These methods can be broken into two parts; reconstruction to the interface, and the Riemann solver.

A wide array of Riemann solvers exist in the literature, but those used in this work are of two families, Roe and HLL. It is expected from other tests that Roe will perform the best, though it is subject to instabilities at low density and high Mach numbers, and HLLD will perform the best of the HLL methods, as it captures more of the eigenstructure of the equations than HLL. However, there does not seem to be a correlation between dissipation and choice of Riemann solver that cannot be explained by some other mechanism. This is not to say that there is no difference, merely not one that can be identified by these data.

The interface reconstruction techniques vary widely among the six schemes, and can primarily be characterized by details discussed in other sections. Namely, order of reconstruction, directional splitting, time integration, and explicit viscosity terms. They will not be discussed further here.

6.4. MHD Methods

Any MHD algorithm is essentially an established hydrodynamic algorithm with modifications to include the Lorentz force in the momentum equation, the induction equation, and some treatment to minimize the divergence of the magnetic field. In all cases in this paper, the Lorentz force is incorporated into the momentum equation directly (rather than through, say, vector potentials). Two of the codes (ENZO and PLUTO) use non-exact divergence preservation, namely both treat an extra wave, in $\nabla \cdot \mathbf{B}$. These methods also include source terms for Equations (1)–(3) that are set to zero in most methods. This extra wave is advected and damped in ENZO, while it is simply advected with the fluid velocity in PLUTO and serves to mitigate singularities in the three-dimensional linearized Jacobian. The rest use a variant of the CT method, wherein the electric field and magnetic field are treated at the zone edge and face, respectively, which allows the solenoidal constraint to be kept zero to machine precision through the curl operator.

One naively expects the two approximate divergence methods to have somewhat higher dissipation than other codes, as the primary driver is dissipation. This is to some extent seen in the data, though PLUTO does not suffer much from this effect as it still has quite high fluid and magnetic Reynolds numbers. ENZO, on the other hand, seems to have more dissipation, and based on its similarity to other spatially second-order codes, the $\nabla \cdot \mathbf{B}$ wave seems to be a likely culprit.

Among the CT-based schemes, the results seem to be dominated by first spatial order then the reconstructed variable. Both PPML and LL-MHD use the electric field reconstruction technique described in the Athena method of Gardiner & Stone (2005), but PPML is spatially third order, so has a higher magnetic Reynolds number. It should be noted that only the electric field reconstruction of the Athena method is used by these methods. FLASH also uses third-order reconstruction, and also has an extremely large magnetic spectral bandwidth. LL-MHD, ZEUS, and RAMSES, on the other hand, are all spatially second order, but ZEUS uses the method of characteristics (MOC), which uses the characteristic fields, and RAMSES solves a second Riemann problem, both of which prove to better capture the electric field than the primitive variable reconstruction used in LL-MHD.

6.5. Three Closely Related Codes

An interesting subset of codes to examine are LL-MHD, RAMSES, and FLASH. These three codes are the most similar in terms of their components, and serve to illustrate how small differences in method details can cause significant differences

in performance. Each of the three codes uses the second-order MUSCL-Hancock reconstruction-evolution scheme for computation of interface states, the HLLD Riemann solver, forward Euler time integration, and a higher-order CT method. Given all the similarities, the differences in performance of the three codes are surprising. This is best shown in the two spectral bandwidth plots in Figure 4. The magnetic bandwidth of FLASH, in Figure 4, right, is the highest of all available codes, as measured by the wavenumber at which the spectrum crosses 75%, with $\log_{10} k/k_{\rm min}$=1.4. RAMSES and LL-MHD are significantly lower, both with $\log_{10} k/k_{\rm min}$=1.1. The spatial order of accuracy in the electric field computation is a clear culprit. FLASH uses a third-order central-difference reconstruction of the electric fields from the Riemann solver. Both RAMSES and LL-MHD, on the other hand, use spatially second-order methods, with RAMSES using a novel two-dimensional Riemann solver, and LL-MHD using the Athena method. This shows the importance of spatial reconstruction in capturing flow features. The velocity bandwidth, in Figure 4, left, is a completely different story: RAMSES is at the high end of the codes, with $\log_{10} k/k_{\rm min}$=1.5, LL-MHD is in the middle, with $\log_{10} k/k_{\rm min}$=1.4, but FLASH is the lowest of the Eulerian codes, with $\log_{10} k/k_{\rm min}$=1.1. This is most interesting, since the base solvers for each of the codes are nearly identical. The biggest difference here is the treatment of directional splitting. RAMSES and FLASH are both directionally unsplit, incorporating transverse derivatives of the Jacobian in the interface reconstruction as discussed in Section 6.6.2, while LL-MHD is split using Strang splitting, and does not include transverse derivatives. This alone does not explain the ordering, as LL-MHD and RAMSES perform quite similarly in many velocity statistics. The only other major algorithmic difference is the inclusion of the longitudinal magnetic derivatives in the FLASH interface reconstruction. It is not obvious that these terms would cause diffusion in the manner observed, though they will affect the reconstruction of the interface states. Finally, each of these methods (indeed all methods described here) include a number of nonlinear switches that determine behavior near shocks, among other things, that have not been explicitly described. Further investigation is required to isolate these finer details.

Due to the tight coupling between velocity and magnetic field in both the momentum and induction equations, it would not be surprising for the velocity and magnetic statistics to be coupled, even perhaps in an inverse manner, through either energy conservation or mode coupling. Thus the higher spatial order used in the FLASH magnetic reconstruction may, for instance, be more efficient at transferring kinetic energy to magnetic energy. Further study is required to definitively pinpoint the cause of differences between these three codes, but it illustrates the effect of seemingly minor details having substantial results on the behavior of a code.

An additional point of interest in the RAMSES behavior is the excess power seen in the spectral bandwidth plot at $\log_{10} k/k_{\rm min} \in [0.8, 1.2]$. This seems to be a manifestation of what in pure hydrodynamic turbulence is referred to as the bottleneck. This is typically not seen in simulations of MHD turbulence at a 512^3 resolution, presumably due to additional effects of non-local MHD mode coupling that allows energy to be more efficiently transferred to smaller scales. As RAMSES has a relatively low Prandtl number, it is possible that this extra energy transfer is not as efficient as in other codes, causing somewhat inflated spectral bandwidth.

6.6. Other Solver Details

There are several other solver design specifications that have received considerable attention over the years. Here we present a discussion of some of the major solver options that have been examined. While each may be crucial in its own right, they are not dominant factors determining the dissipation properties studied here.

6.6.1. Evolved Variables

MHD can be described by three distinct sets of variables: primitive variables (ρ, $\mathbf{u}$, $\mathbf{B}$, $p_{\rm tot}$), conserved variables (ρ, $\rho\mathbf{u}$, $\mathbf{B}$, $E_{\rm tot}$), and the characteristic variables, R^k, which are the eigenvectors of the Jacobian of the equations, and in some ways the most physically relevant form of the variables. It has been shown that in some cases working with the characteristic variables gives superior results to the other two (Balsara 2004). There is some evidence that bears this out in these data. For instance, the magnetic behavior of ZEUS, in which MOC traces characteristics to compute the electric field, is generally less dissipative than LL-MHD, which uses primarily primitive variables. However, this is not universally the case, and other factors may prove more important. Such is the case in the velocity performance of FLASH versus RAMSES, which use spatial limiting on characteristic and primitive variables, respectively.

6.6.2. Directional Splitting

Computational algorithms have a long history of being developed as one-dimensional methods. They then must be extended by some manner to three dimensions. There are essentially three categories of multidimensional techniques employed by the codes in this study: directly unsplit, directionally split, and transverse flux methods.

The two directionally split methods (LL-MHD and ZEUS) employ sequential one-dimensional solutions along each coordinate axis, wherein the partial update of one sweep is used as the initial data for the following sweep. The order of sweeps in both methods is permuted to reduce error. In both methods, the electric field is computed after the three sweeps are finished.

The four "directly unsplit" methods are STAGGER, KT-MHD, PLUTO, and ENZO. The first two do not rely on strictly one-dimensional techniques, so they employ fully three-dimensional evolution by repeated application of the interpolation and derivative operators. The ENZO and PLUTO methods use the Godunov method, which is strictly speaking one-dimensional as will be discussed below. It applies the algorithm in an unsplit fashion, with the initial state for Riemann solutions coming from the same data for all three dimensions. It incorporates multidimensional properties of the flow by way of the Runge–Kutta integration.

Another unsplit technique, dubbed "transverse reconstruction" here, is used to incorporate three-dimensional terms into the finite-volume methods. Godunov's method is, strictly speaking, one-dimensional, and does not lend itself directly to multidimensional techniques. The underlying one-dimensional method follows three basic steps: reconstruction of two interface states at each zone boundary, followed by solution of the Riemann problem at the zone boundary, and finally using that solution to compute difference fluxes at the interface to update the field. Three of the schemes (FLASH, PPML, and RAMSES) introduce the multidimensional terms in the reconstruction of the interface state, through the addition of terms approximating gradients of the transverse fluxes, $\partial F_y/\partial y$. The techniques vary

slightly between the four methods. FLASH and RAMSES use a linearization of the transverse flux gradient, $A_y \partial U/\partial y$, to compute the half step advance in time. Here, A_y is the Jacobian of the flux, and the derivative is approximated with monotonized central differences. PLUTO uses a full reconstruction and Riemann solution in the transverse direction. PPML also includes a linearization of the transverse flux, though it is incorporated slightly differently, with the transverse flux gradient introduced in the characteristic invariants, and uses characteristic direction filtering for upwinding the derivative.

While it is often believed that directional sweeping is a detriment to the solution quality, the metrics presented in this work do not show a clear correlation between the different multidimensional techniques.

6.6.3. Time Integration

In principle, the order of the spatial and temporal integration should be the same, otherwise the convergence properties of the scheme will be reduced to the lower of the two. However, time integration in these cases seems to be dwarfed by other effects. ENZO is of higher order in time than RAMSES, but significantly more dissipative. Similarly, PLUTO is higher order in time than PPML, but typically has higher dissipation, as well.

7. SUMMARY AND CONCLUSIONS

We have compared nine numerical MHD codes on a decaying supersonic, super-Alfvénic turbulence test problem with conditions similar to star-forming molecular clouds in the Galaxy. The codes ENZO, FLASH, KT-MHD, LL-MHD, PLUTO, PPML, RAMSES, STAGGER, and ZEUS, described in detail in Section 2, employ a variety of numerical algorithms of varying order of accuracy, multidimensional and time integration schemes, shock capturing techniques, and treatment of the solenoidal constraint on the magnetic field. Together, they represent a majority of the MHD codes in use in numerical astrophysics today and therefore sample the current state of the art. The work presented in this paper is the largest, most comprehensive MHD code comparison on an application-like test problem to date.

The codes were compared using both integrated and spectral measures of the velocity and magnetic fields. All nine Eulerian codes agreed surprisingly well on the kinetic energy decay rate (Figure 1, top left), which indicates both the robustness of published predictions (Mac Low et al. 1998; Stone et al. 1998; Lemaster & Stone 2009) as well as the inadequacy of this particular metric as a discriminant among methods. All nine Eulerian codes likewise agreed on the magnetic energy decay rate (Figure 1, top right), but varied on the amplitude of the peak magnetic energy as this proved sensitive to the effective magnetic Reynolds number of the simulation, which depends on the numerical dissipation of the method.

To move beyond simple global energy diagnostics, small-scale kinetic and magnetic field diagnostics were introduced in order to empirically measure the effective fluid and magnetic Reynolds numbers of the various codes. These diagnostics are based on analytically motivated combinations of the volume integrated fluid enstrophy, dilatation, and square of the electric current density (Figure 2). They proved more revealing about the numerical dissipation present in the various methods, and motivated a closer investigation using power spectra of the velocity and magnetic fields. Regarding the latter, the concept of effective spectral bandwidth (ESB) was introduced as a quantitative metric for code comparison. The effective spectral bandwidth is defined as the width in wavenumber space where the numerical results do not deviate from a reference solution (typically, a higher resolution simulation) by more than 25%. The ESB was measured for both the velocity and magnetic power spectra for all nine codes at reference times during the decay. A detailed comparison of ESBs leads to several general conclusions and observations.

1. All codes gave qualitatively the same results, implying that they are all performing reasonably well and are useful for scientific investigations.
2. No single code outperformed all the others against all metrics, although in general higher-order-accurate methods do better than lower-order-accurate methods. The lack of a clear winner stems from the fact that a single MHD code is a combination of many different algorithms representing specific design choices, and that many combinations are possible.
3. The spatial order of accuracy is the primary determinant of velocity spectral bandwidth and effective Reynolds number. Higher spatial order correlates to higher spectral bandwidth. The sixth-order code STAGGER is superior to the third-order codes PPML, PLUTO, KT-MHD, and FLASH, which are superior to the second-order codes ZEUS, LL-MHD, and ENZO.
4. Codes with high velocity spectral bandwidth do not necessarily have high magnetic spectral bandwidth. For example, the STAGGER code has the highest velocity ESB but the lowest magnetic ESB. The magnetic ESB is sensitive to the spatial order of accuracy of the electric field computation, and is higher in methods that interpolate on characteristic variables as opposed to primitive variables.
5. The use of explicit artificial viscosity to stabilize shock waves reduces the velocity spectral bandwidth relative to methods that do not use artificial viscosity, such as Godunov methods.
6. The use of explicit divergence cleaning reduces the magnetic spectral bandwidth relative to codes that preserve the solenoidal condition on **B** exactly (CT methods).
7. Other algorithmic choices such as finite-difference versus finite-volume discretization, directionally split versus unsplit updates of the conservations laws, and order of accuracy of the time integration are less well correlated with the performance metrics, and therefore appear to be less important in predicting a code's behavior on MHD turbulence.

Observations about specific codes are as follows.

1. The best performers overall are PPML, FLASH, PLUTO, and RAMSES based on velocity and magnetic Reynolds numbers and spectral bandwidths.
2. The highest fluid Reynolds number was obtained with the STAGGER code.
3. The highest magnetic Prandtl number was obtained with the FLASH code.
4. FLASH is somewhat more diffusive on the hydro part than its magnetic part, and the reverse is true for the RAMSES code.
5. The dilatation velocity power spectra of KT-MHD and ENZO exhibit problematic behavior on small scales that is likely related to the ways these codes maintain $\nabla \cdot \mathbf{B} = 0$.

The best performing codes employ a consistently high order of accuracy for spatial reconstruction of the evolved fields, transverse gradient interpolation, conservation law update step, and Lorentz force computation. Three of the four employ divergence-free evolution of the magnetic field using the CT method, and all use little to no explicit artificial viscosity. These would seem to be guidelines for the development of future schemes. Codes that fall short in one or more of these areas are still useful, but they must compensate higher numerical dissipation with higher numerical resolution. A new class of nearly Lagrangian methods for hydrodynamics has recently emerged which uses a moving mesh based on Voronoi cells (Springel 2010). It remains to be seen if this approach can be generalized to MHD while retaining the beneficial elements of successful Eulerian schemes.

This work was prepared in part during the workshop "Star Formation Through Cosmic Time" at the KITP in Santa Barbara, and was supported in part by the National Science Foundation under grant no. PHY05-51164. Computer support for this project was partly provided by the San Diego Supercomputer Center, through an LRAC supercomputer allocation in support of the Computational Astrophysics Data Analysis Center. A.K. was supported in part by the National Science Foundation under grants AST0507768, AST0607675, AST0808184, and AST0908740. D.C. was supported in part by the National Science Foundation under grants AST0808184, and AST0908740. D.C. and H.X. were supported in part by Los Alamos National Laboratory, LLC for the National Nuclear Security Administration of the U.S. Department of Energy under contract DE-AC52-06NA25396. Simulations with ENZO and PPML utilized NSF TeraGrid resources provided by SDSC, NICS, and TACC through allocation MCA07S014. Å.N. was supported in part by the Danish Natural Research Council. STAGGER code results were computed at the University of Copenhagen node of the Danish Center for Scientific Computing. P.P. is supported by MICINN (Spanish Ministry for Science and Innovation) grant AYA2010-16833 and by the FP7-PEOPLE-2010-RG grant PIRG07-GA-2010-261359. R.B. was funded during this research by the Deutsche Forschungsgemeinschaft under grant KL1358/4-1. C.F. has received funding from the European Research Council under the European Community's Seventh Framework Programme (FP7/2007-2013 grant agreement no. 247060) for the research presented in this work. The FLASH simulations were run at the Leibniz Rechenzentrum (grant pr32lo) and the Jülich Supercomputing Centre (grant hhd20). The FLASH code has been developed by the DOE-supported ASC/Alliance Center for Astrophysical Thermonuclear Flashes at the University of Chicago. D.L. was supported by the U.S. Department of Energy under grant no. B523820 to the Center for Astrophysical Thermonuclear Flashes at the University of Chicago. M.F. thanks Andrea Mignone and Natalia Dzyurkevich for their comments on this test. The PLUTO calculation was done on the "Theo" cluster of MPIA Heidelberg. P.S.L. is supported by the NASA ATFP grants NNG06-GH96G and NNX09AK31G. Work of C.V. and W.C.M. was supported by the DFG cluster of excellence: Origin and Structure of the Universe. The RAMSES simulations were performed thanks to the HPC resources of CCRT under the allocations 2009-SAP2191 and 2010-GEN2192 made by GENCI, France. The authors are grateful to the anonymous referee for a prompt and constructive review.

REFERENCES

Archontis, V., Dorch, S. B. F., & Nordlund, Å. 2007, A&A, 472, 715
Asplund, M., Ludwig, H.-G., Nordlund, Å., & Stein, R. F. 2000, A&A, 359, 669
Balbás, J., & Tadmor, E. 2006, SIAM J. Sci. Comput., 28, 533
Balsara, D. S. 2004, ApJS, 151, 149
Balsara, D. S., & Shu, C.-W. 2000, J. Comput. Phys., 160, 405
Barth, T. J. 1990, VKI, Comput. Fluid Dyn., 2, 66
Benzi, R., Biferale, L., Fisher, R. T., Kadanoff, L. P., Lamb, D. Q., & Toschi, F. 2008, Phys. Rev. Lett., 100, 234503
Biskamp, D. 2003, Magnetohydrodynamic Turbulence (Cambridge: Cambridge Univ. Press)
Braithwaite, J., & Nordlund, Å. 2006, A&A, 450, 1077
Brandenburg, A., & Nordlund, A. 2011, Rep. Prog. Phys., 74, 046901
Čada, M., & Torrilhon, M. 2009, J. Comput. Phys., 228, 4118
Colella, P. 1990, J. Comput. Phys., 87, 171
Colella, P., & Woodward, P. R. 1984, J. Comput. Phys., 54, 174
Collins, D. C., Padoan, P., Norman, M. L., & Xu, H. 2011, ApJ, 731, 59
Collins, D. C., Xu, H., Norman, M. L., Li, H., & Li, S. 2010, ApJS, 186, 308
Dedner, A., Kemm, F., Kröner, D., Munz, C.-D., Schnitzer, T., & Wesenberg, M. 2002, J. Comput. Phys., 175, 645
Dobler, W., Haugen, N. E., Yousef, T. A., & Brandenburg, A. 2003, Phys. Rev. E, 68, 026304
Dreher, J., & Grauer, R. 2005, Parallel Comput., 31, 913
Dubey, A., et al. 2008, in ASP Conf. Ser. 385, Numerical Modeling of Space Plasma Flows, ed. N. V. Pogorelov, E. Audit, & G. P. Zank (San Francisco, CA: ASP), 145
Falgarone, E., Puget, J.-L., & Perault, M. 1992, A&A, 257, 715
Falkovich, G. 1994, Phys. Fluids, 6, 1411
Federrath, C., Klessen, R. S., & Schmidt, W. 2008, ApJ, 688, L79
Federrath, C., Roman-Duval, J., Klessen, R. S., Schmidt, W., & Mac Low, M.-M. 2010, A&A, 512, A81
Federrath, C., Sur, S., Schleicher, D. R. G., Banerjee, R., & Klessen, R. S. 2011, ApJ, 731, 62
Fromang, S., Hennebelle, P., & Teyssier, R. 2006, A&A, 457, 371
Fryxell, B., et al. 2000, ApJS, 131, 273
Galsgaard, K. 1996, PhD thesis, Univ. Copenhagen
Galsgaard, K., & Nordlund, Å. 1996, J. Geophys. Res., 101, 13445
Gardiner, T. A., & Stone, J. M. 2005, J. Comput. Phys., 205, 509
Grinstein, F., Margolin, L., & Rider, W. (ed.) 2007, Implicit Large-Eddy Simulation: Computing Turbulent Fluid Dynamics (Cambridge: Cambridge Univ. Press)
Gudiksen, B. V., & Nordlund, Å. 2005, ApJ, 618, 1020
Harten, A., Lax, P. D., & van Leer, B. 1983, SIAM Rev., 25, 35
Haugen, N. E., & Brandenburg, A. 2004, Phys. Rev. E, 70, 026405
Haugen, N. E. L., Brandenburg, A., & Mee, A. J. 2004, MNRAS, 353, 947
Hawley, J. F., & Stone, J. M. 1995, Comput. Phys. Commun., 89, 127
Hayes, J. C., Norman, M. L., Fiedler, R. A., Bordner, J. O., Li, P. S., Clark, S. E., ud-Doula, A., & Mac Low, M.-M. 2006, ApJS, 165, 188
Hennebelle, P., & Chabrier, G. 2008, ApJ, 684, 395
Hennebelle, P., & Chabrier, G. 2009, ApJ, 702, 1428
Heyer, M. H., & Brunt, C. M. 2004, ApJ, 615, L45
Johnsen, E., et al. 2010, J. Comput. Phys., 229, 1213
Jones, T. W., Porter, D. H., Ryu, D., & Cho, J. 2011, arXiv:1101.4050
Kissmann, R. 2006, Numerical Investigation of the Turbulent ISM, PhD thesis, Ruhr-Universität Bochum
Kitsionas, S., et al. 2009, A&A, 508, 541
Klessen, R. S., Krumholz, M. R., & Heitsch, F. 2009, arXiv:0906.4452
Kritsuk, A. G., Norman, M. L., & Padoan, P. 2006, ApJ, 638, L25
Kritsuk, A. G., Norman, M. L., Padoan, P., & Wagner, R. 2007, ApJ, 665, 416
Kritsuk, A. G., Ustyugov, S. D., & Norman, M. L. 2011, in Proc. IAU Symp. 270, Computational Star Formation, ed. J. Alves, B. Elmegreen, & V. Trimble (Cambridge: Cambridge Univ. Press), 179
Kritsuk, A. G., Ustyugov, S. D., Norman, M. L., & Padoan, P. 2009a, in ASP Conf. Ser. 406, Numerical Modeling of Space Plasma Flows, ed. N. V. Pogorelov, E. Audit, P. Colella, & G. P. Zank (San Francisco, CA: ASP), 15
Kritsuk, A. G., Ustyugov, S. D., Norman, M. L., & Padoan, P. 2009b, J. Phys.: Conf. Ser., 180, 012020
Kritsuk, A. G., Ustyugov, S. D., Norman, M. L., & Padoan, P. 2010, in ASP Conf. Ser. 429, Numerical Modeling of Space Plasma Flows, ed. N. V. Pogorelov, E. Audit, & G. P. Zank (San Francisco, CA: ASP), 15
Krumholz, M. R., & McKee, C. F. 2005, ApJ, 630, 250
Krumholz, M. R., & Tan, J. C. 2007, ApJ, 654, 304
Kurganov, A., & Tadmor, E. 2000, J. Comput. Phys., 160, 241
Laney, C. B. 1998, Computational Gasdynamics (Cambridge: Cambridge Univ. Press)

Larson, R. B. 1981, MNRAS, 194, 809
Lee, D., & Deane, A. E. 2009, J. Comput. Phys., 228, 952
Lele, S. K., Larsson, J., Bhagatwala, A., & Moin, P. 2009, in ASP Conf. Ser. 406, Numerical Modeling of Space Plasma Flows, ed. N. V. Pogorelov, E. Audit, P. Colella, & G. P. Zank (San Francisco, CA: ASP), 31
Lemaster, M. N., & Stone, J. M. 2009, ApJ, 691, 1092
LeVeque, R. J. 2002, Numerical Methods for Conservation Laws (Cambridge: Cambridge Univ. Press)
Li, S., Li, H., & Cen, R. 2008, ApJS, 174, 1
Londrillo, P., & del Zanna, L. 2004, J. Comput. Phys., 195, 17
Lunttila, T., Padoan, P., Juvela, M., & Nordlund, Å. 2008, ApJ, 686, L91
Lunttila, T., Padoan, P., Juvela, M., & Nordlund, Å. 2009, ApJ, 702, L37
Low, M.-M., & Klessen, R. S. 2004, Rev. Mod. Phys., 76, 125
Mac Low, M.-M., Klessen, R. S., Burkert, A., & Smith, M. D. 1998, Phys. Rev. Lett., 80, 2754
McKee, C. F., & Ostriker, E. C. 2007, ARA&A, 45, 565
Mignone, A. 2007, J. Comput. Phys., 225, 1427
Mignone, A. 2009, Mem. Soc. Astron. Ital. Suppl., 13, 67
Mignone, A., & Tzeferacos, P. 2010, J. Comput. Phys., 229, 2117
Mignone, A., Tzeferacos, P., & Bodo, G. 2010, J. Comput. Phys., 229, 5896
Miyoshi, T., & Kusano, K. 2005, J. Comput. Phys., 208, 315
O'Shea, B. W., Bryan, G., Bordner, J., Norman, M. L., Abel, T., Harkness, R., & Kritsuk, A. 2005, in Lecture Notes in Computational Science and Engineering 41, Adaptive Mesh Refinement – Theory and Applications, ed. T. Plewa, T. Linde, & V. G. Weirs (Berlin: Springer), 341
Padoan, P., Jimenez, R., Nordlund, Å., & Boldyrev, S. 2004, Phys. Rev. Lett., 92, 191102
Padoan, P., Juvela, M., Bally, J., & Nordlund, A. 1998, ApJ, 504, 300
Padoan, P., Kritsuk, A. G., Lunttila, T., Juvela, M., Nordlund, A., Norman, M. L., & Ustyugov, S. D. 2010, in AIP Conf. Ser. 1242, Plasmas in the Laboratory and the Universe: Interactions, Patterns, and Turbulence, ed. G. Bertin et al. (Melville, NY: AIP), 219
Padoan, P., & Nordlund, Å. 1999, ApJ, 526, 279
Padoan, P., & Nordlund, Å. 2002, ApJ, 576, 870
Padoan, P., & Nordlund, A. 2011, ApJ, 730, 40
Padoan, P., Nordlund, A., & Jones, B. J. T. 1997, MNRAS, 288, 145
Padoan, P., Nordlund, Å., Kritsuk, A. G., Norman, M. L., & Li, P. S. 2007, ApJ, 661, 972
Padoan, P., Zweibel, E., & Nordlund, Å. 2000, ApJ, 540, 332
Pan, L., Padoan, P., & Kritsuk, A. G. 2009, Phys. Rev. Lett., 102, 034501
Porter, D. H., Pouquet, A., & Woodward, P. R. 2002, Phys. Rev. E, 66, 026301
Powell, K. G., Roe, P. L., Linde, T. J., Gombosi, T. I., & de Zeeuw, D. L. 1999, J. Comput. Phys., 154, 284
Price, D. J., & Federrath, C. 2010, MNRAS, 406, 1659
Pudritz, R. E. 2011, in IAU Symp. 270, Computational Star Formation, ed. J. Alves, B. Elmegreen, & V. Trimble (Cambridge Univ. Press), 151
Rider, W. J., Greenough, J. A., & Kamm, J. R. 2007, J. Comput. Phys., 225, 1827
Rosolowsky, E. W., Pineda, J. E., Kauffmann, J., & Goodman, A. A. 2008, ApJ, 679, 1338
Shu, C.-W., & Osher, S. 1988, J. Comput. Phys., 77, 439
Springel, V. 2010, MNRAS, 401, 791
Stein, R. F., Lagerfjärd, A., Nordlund, Å., & Georgobiani, D. 2011, Sol. Phys., 268, 271
Stein, R. F., & Nordlund, A. 1998, ApJ, 499, 914
Stone, J. M., & Norman, M. L. 1992a, ApJS, 80, 753
Stone, J. M., & Norman, M. L. 1992b, ApJS, 80, 791
Stone, J. M., Ostriker, E. C., & Gammie, C. F. 1998, ApJ, 508, L99
Suresh, A., & Huynh, H. T. 1997, J. Comput. Phys., 136, 83
Sytine, I. V., Porter, D. H., Woodward, P. R., Hodson, S. W., & Winkler, K.-H. 2000, J. Comput. Phys., 158, 225
Teyssier, R. 2002, A&A, 385, 337
Teyssier, R., Fromang, S., & Dormy, E. 2006, J. Comput. Phys., 218, 44
Toro, E. 1999, Riemann Solvers and Numerical Methods for Fluid Dynamics: A Practical Introduction (Berlin: Springer)
Ustyugov, S. D., Popov, M. V., Kritsuk, A. G., & Norman, M. L. 2009, J. Comput. Phys., 228, 7614
van Leer, B. 1979, J. Comput. Phys., 32, 101
van Leer, B. 1977, J. Comput. Phys., 23, 276
Wang, P., & Abel, T. 2009, ApJ, 696, 96
Wang, P., Abel, T., & Zhang, W. 2008, ApJS, 176, 46
Xu, H., Li, H., Collins, D. C., Li, S., & Norman, M. L. 2010, ApJ, 725, 2152
Ziegler, U. 2004, J. Comput. Phys., 196, 393